# Rayleigh–Bénard convection in the presence of spatial temperature modulations

## G. FREUND, W. PESCH† AND W. ZIMMERMANN

Institute of Physics, University of Bayreuth, D-95440 Bayreuth, Germany

Motivated by recent experiments, we study a rich variation of the familiar Rayleigh–Bénard convection (RBC), where the temperature at the lower boundary varies sinusoidally about a mean value. As usual the Rayleigh number $R$ measures the average temperature gradient, while the additional spatial modulation is characterized by a (small) amplitude $\delta_m$ and a wavevector $\boldsymbol{q}_m$. Our analysis relies on precise numerical solutions of suitably adapted Oberbeck–Boussinesq equations (OBE). In the absence of forcing ($\delta_m = 0$), convection rolls with wavenumber $q_c$ bifurcate only for $R$ above the critical Rayleigh number $R_c$. In contrast, for $\delta_m \neq 0$, convection is unavoidable for any finite $R$; in the most simple case in the form of 'forced rolls' with wavevector $\boldsymbol{q}_m$. According to our first comprehensive stability diagram of these forced rolls in the $q_m - R$ plane, they develop instabilities against resonant *oblique* modes at $R \lesssim R_c$ in a wide range of $q_m/q_c$. Only for $q_m$ in the vicinity of $q_c$, the forced rolls remain stable up to fairly large $R > R_c$. Direct numerical simulations of the OBE support and extend the findings of the stability analysis. Moreover, we are in line with the experimental results and also with some earlier theoretical results on this problem, based on asymptotic expansions in the limit $\delta_m \to 0$ and $R \to R_c$. It is satisfying that in many cases the numerical results can be directly interpreted in terms of suitably constructed amplitude and generalized Swift–Hohenberg equations.

**Key words:** Bénard convection, nonlinear instability, pattern formation

## 1. Introduction

Non-equilibrium phase transitions in systems with translational invariance often give rise to spatially periodic stripe patterns of wavevector $\boldsymbol{q}$. A paradigmatic and intensely studied example is Rayleigh–Bénard convection (RBC; see for instance Bodenschatz, Pesch & Ahlers 2000) in a thin horizontal fluid layer subjected to a transverse temperature gradient, which is parametrized by the Rayleigh number $R$. This system is rotationally invariant in the plane of the fluid layer and the onset of convection is characterized by a parabolic linear stability curve (or neutral curve) $R_0(q)$ in the parameter space spanned by $R$ and the wavenumber $q$. The neutral curve has its minimum at the critical wavenumber $q = q_c$, with the critical Rayleigh number, $R_c = R_0(q_c)$. For $R$ above $R_0(q)$ periodic roll solutions exist, which are degenerate with respect to rotations of $\boldsymbol{q}$. Exploring the stability regime of rolls (the famous 'Busse balloon') in experiments is a demanding task. Even more difficult is the problem of

† Email address for correspondence: werner.pesch@uni-bayreuth.de

pattern selection, i.e. to understand which state within the Busse balloon is actually spontaneously chosen by the system dynamics in a specific experiment. In some cases we have even competition between rolls and spatio-temporally chaotic states like spiral-defect chaos (see for instance Bodenschatz *et al.* 2000, in particular figure 5 therein).

Such problems can be tackled by imposing an external spatial modulation with wavevector $q_m$ onto a system, which allows to control, besides $R$, the wavevector of the resulting patterns. For instance, in Busse & Whitehead (1971) unstable initial roll patterns with $R, q$ values outside the Busse balloon have been 'imprinted' by an optical forcing method. After shutting down the forcing, their evolution towards the stable roll regime has been followed. The system thus exhibits well-understood destabilization mechanism like the zigzag, the cross-roll and the skewed-varicose instabilities (Busse & Clever 1979). An analogous approach has been devoted to hexagonal patterns in Bénard–Marangoni convection (Semwogerere & Schatz 2002).

Furthermore, we mention the use of a spatially periodic modulation of the applied voltage in experiments on planar electro-convection (Lowe & Gollub 1985*a,b*; Henriot, Burguete & Ribotta 2003). Besides an improved understanding of the stability regimes of rolls, the appearance of incommensurate states characterized by soliton-like phase disturbances is of particular interest (Lowe & Gollub 1985*b*).

To our best knowledge, the first experiments on steadily forced RBC with $q_m \approx q_c$ have been performed only recently (McCoy 2008; McCoy *et al.* 2008; Seiden *et al.* 2008; Weiss 2009). Here, the distance $d$ between the horizontal plates confining the convection cell has been periodically modulated by gluing an array of equidistant polymer stripes of height $h \ll d$ on the inner surface of the lower plate. The average layer height $d$ can be varied to some extent and thus $q_c \sim d^{-1}$ as well, which allows exploration of forced rolls with wavenumbers $q_m$ in a finite interval about $q_c$. The experiments present a wealth of new phenomena, whose detailed analysis has just started. One observes, in particular, transitions from forced two-dimensional roll patterns to fascinating three-dimensional ones in Seiden, Weiss & Bodenschatz (2009). In addition, the typical transitions to spatio-temporally chaotic patterns, which would appear in the absence of modulation, are suppressed in this case.

There are good theoretical arguments (Kelly & Pal 1978; Seiden *et al.* 2008) that the geometrical boundary modulation in the RBC experiments can be satisfactorily mapped onto a pure temperature modulation at the lower plate with a small amplitude $\delta_m \sim O(0.01)$. We have thus restricted ourselves in this paper to a temperature modulation model, which is much easier to analyse than the geometrical modulations.

Only very few approximate theoretical investigations of periodically modulated RBC for $q_m \approx q_c$ exist in the literature. They are based on asymptotic expansions in the limits $R \to R_c$ and $\delta_m \to 0$. Unfortunately, the first analysis of Vozovoi & Nepomnyashchy (1974) remained largely unnoticed since it appeared in a barely accessible Russian publication. They arrived at the standard amplitude equation of RBC modified by an additive correction, such that the familiar forward bifurcation to rolls in RBC transforms into an *imperfect bifurcation*. This result has been confirmed in an independent, more general analysis of the problem by Kelly & Pal (1978) (see also Kelly & Pal 1976 and the review of Kelly 1993). The *stability* of forced rolls in the limit $\delta_m \to 0$ and $R \approx R_c$ has also been investigated by Vozovoi & Nepomnyashchy (1974) in particular for $q_m \approx q_c$ and by Pal & Kelly (1979) for $q_m$ away from $q_c$. In these papers, the importance of *oblique* destabilizing modes with wavevector $s$ ($s \approx q_c$)

not parallel to $q_m$ has been emphasized. Such modes are not covered by the very interesting quasi-two-dimensional analysis of RBC in terms of Ginzburg–Landau equations by Coullet & Huerre (1986), which has thus no direct relation to the present work. This also applies to the exact two-dimensional analysis of modulated RBC in Schmitz & Zimmermann (1996), in particular since only the limit $q_m \ll q_c$ was considered there.

The main goal of the present work is to provide a rigorous theoretical analysis of rolls and their stability in the presence of forcing with small amplitude $\delta_m$ and in a wide range of ratios $q_m/q_c$. The investigation covers the recent experiments with $\delta_m \sim O(0.01)$ and $q_m \approx q_c$. The analysis of the underlying Oberbeck–Boussinesq equations (OBE) including the external modulation is based on Galerkin methods and the first direct numerical simulations of forced RBC. They show a large variety of patterns, which are not known from unforced RBC.

Our forced roll solutions are consistent with the previous approximate results for $R \approx R_c$ and for $q_m \approx q_c$ by Vozovoi & Nepomnyashchy (1974) and Kelly & Pal (1978). The stability of the forced rolls strongly depends on the ratio $q_m/q_c$. If the modulation wavenumber $q_m$ is chosen in the interior of a 'gap of instability', $q_l \lesssim q_m \lesssim q_u$, where $q_l \approx 0.8\,q_c$ and $q_u \approx 1.2\,q_c$ for $\delta_m = 0.01$ and $Pr = 1$, the forced roll solutions are stable up to Rayleigh numbers that are considerably larger than $R_c$, in agreement with the recent experiments (McCoy *et al.* 2008; Seiden *et al.* 2008). The limiting curves of the stability diagram in this regime closely follow those of non-modulated RBC with increasing $R$, except that some typical long-wavelength instabilities (such as Eckhaus and zigzag) are suppressed. These are generically related to the translational invariance of standard RBC, which is obviously absent for finite $\delta_m$. Outside the gap of instability, for $0 < q_m < q_l$ or $q_u < q_m < 2q_c$, the forced rolls become unstable for $R > R_{ob}$ with $R_{ob} \lesssim R_c$, against oblique modes with wavevectors $s_{1,2} = (q_m/2, \pm p)$, where $(q_m/2)^2 + p^2 = q_c^2$, as suggested by Vozovoi & Nepomnyashchy (1974) and Pal & Kelly (1979). We find that for $R \gtrsim R_{ob}$ this instability leads to *rectangular* patterns, characterized by a superposition of the two degenerate oblique modes with wavevectors $s_{1,2}$. These patterns have no counterpart in non-modulated RBC. For $q_m > 2q_c$, the destabilization of the forced rolls is typically governed by transverse modes with wavevector $s = (0, q_c)$. Finally, we would like to stress that our interpretation of the various bifurcation scenarios and the ensuing patterns in the weakly nonlinear regime has greatly benefited from the analysis of suitable amplitude and Swift–Hohenberg equations.

This paper is organized as follows. In §2 we provide the theoretical background of the paper. After the formulation of the pertaining OBE, we sketch the methods to solve them. The following §3 is devoted to the presentation of the forced roll solutions with wavenumber $q_m$ and to a careful comparison with the amplitude equations of Vozovoi & Nepomnyashchy (1974) and Kelly & Pal (1978). In §4 we use Galerkin methods to capture the destabilization of the forced rolls, which is driven by a variety of modes characterized by different wavevectors $s$. The numerical results in §4 are elucidated and confirmed in §5 by a quasi-analytical amplitude-equation approach. Section 6 deals with the patterns that develop after the destabilization of the forced roll solution. We discuss selected results obtained by direct numerical simulations of the OBE and focus in particular on patterns arising from the oblique-roll bifurcation. Furthermore, it is demonstrated that additional insight into the various aspects of modulated thermal convection can be gained from a suitably chosen Swift–Hohenberg model, whose analysis is much less demanding than that of the full OBE. The paper closes with some concluding remarks and an outlook to future work in §7. The

Appendix is devoted to the derivation of the various amplitude equations exploited in this paper and to the calculation of their coefficients.

## 2. Theoretical description

In §2.1, the OBE are generalized to the case of a spatially modulated temperature profile at the lower plate. Then, §2.2 deals with a short description of the Galerkin analysis we have employed to construct the stationary forced roll solutions and to examine their stability. In addition, we sketch our method for direct simulations of the OBE.

### 2.1. *Basic equations*

The familiar set-up for RBC consists of a fluid layer (parallel to the $x$–$y$ plane) of thickness $d$ and lateral extension $L$. The layer is heated from below (temperature $T_1$) and cooled from above (temperature $T_2 < T_1$). The resulting temperature gradient is thus parallel to the vertical unit vector $e_z$ and anti-parallel to gravity $-ge_z$. The system is described by the standard OBE for the temperature field $T(x, z, t)$ and the velocity field $u(x, z, t)$, where $x = (x, y)$ denotes the horizontal coordinates.

In the present work, we focus on a particular variant of standard RBC, where the temperature at the lower plate varies sinusoidally in space around an average value $T_1$. This situation is described by the following boundary conditions for the temperature:

$$T = T_2 \quad \text{at} \quad z = \frac{d}{2}, \quad T = \bar{T} + \frac{\Delta T}{2}[1 + 2\delta_m \cos(q_m \cdot x)] \quad \text{at} \quad z = -\frac{d}{2}. \quad (2.1)$$

Here, $\bar{T} = (T_1 + T_2)/2$ denotes the mean temperature and $\Delta T = T_1 - T_2 > 0$ denotes the average temperature difference across the layer. The externally imposed temperature modulation at the lower plate is characterized by the modulation wavevector $q_m$ and the modulation amplitude $\delta_m$. Without loss of generality, we choose the $x$-axis of our coordinate frame parallel to the direction of modulation ($q_m = q_m e_x$).

To reformulate the OBE in terms of dimensionless quantities (denoted by primes), we follow the standard convention in choosing $d$ as length scale and $d^2/\kappa$ as time scale, where $\kappa$ is the thermal diffusivity of the fluid. The temperature is measured in units of $T_s = \nu\kappa/\alpha g d^3$, with the thermal expansion coefficient $\alpha$ and the kinematic viscosity $\nu$. All material parameters are taken at $T = \bar{T}$. The pressure scale is given by $\rho_0 \nu\kappa/d^2$, with $\rho_0$ being the density at $T = \bar{T}$. The material parameters can be lumped into two dimensionless quantities, the Rayleigh number $R$ and the Prandtl number $Pr$,

$$R = \alpha g d^3 \Delta T/(\nu\kappa) = \Delta T/T_s, \quad Pr = \nu/\kappa. \quad (2.2)$$

Similar to Vozovoi & Nepomnyashchy (1974) and Kelly & Pal (1978), the dimensionless temperature $T' = T/T_s$ is decomposed into a 'quasi-conductive' contribution, $T'_{cond}$, which fulfils the boundary conditions (2.1), and a 'convective' contribution, $\theta$, which vanishes at $z = \pm d/2$. This is achieved by the ansatz

$$T'(x', z') = T'_{cond}(x', z') + \theta(x', z'), \quad (2.3a)$$

with $x' = x/d, z' = z/d$ and

$$T'_{cond}(x', z') = \frac{R}{\Delta T} \left[ \bar{T} - \Delta T z' + \Delta T \, \delta_m T'_m(x', z') \right]. \quad (2.3b)$$

It is advantageous to fix $T'_m(x', z')$ by requiring $\nabla'^2 T'_m = 0$, which leads to

$$T'_m(x', z') = 2\cos(q'_m x')\, t_m(q'_m, z'), \tag{2.4}$$

where

$$t_m(q'_m, z') = \frac{1}{2} \frac{\sinh[q'_m(1/2 - z')]}{\sinh(q'_m)} \tag{2.5a}$$

and

$$q'_m = \frac{q_m}{d}. \tag{2.5b}$$

In the following, we will always refer to dimensionless quantities; consequently, the primes are suppressed. Using the ansatz (2.3), the non-dimensional OBE for $\theta$ and the velocity $u$ read

$$\frac{\partial \theta}{\partial t} + (u \cdot \nabla)\theta = \nabla^2 \theta - R u_z - \delta_m R(u \cdot \nabla)\, T_m(x, z), \tag{2.6a}$$

$$\frac{1}{Pr}\left(\frac{\partial u}{\partial t} + (u \cdot \nabla)u\right) = \nabla^2 u + e_z\,[\theta + \delta_m\, R T_m(x, z)] - \nabla \Pi, \tag{2.6b}$$

$$\nabla \cdot u = 0, \tag{2.6c}$$

where some gradient terms have been absorbed in the pressure $\Pi$. The terms $\propto \delta_m$ capture the effect of the temperature modulation. For small $\delta_m$ and $R$ sufficiently below $R_c$ (termed as 'quasi-conductive' regime by Kelly & Pal 1978), the *additive*, linear-in-$\delta_m$ correction of the buoyancy term in (2.6b) dominates the *multiplicative* correction due to the advection of $T_m$ in (2.6a), which produces terms $O(\delta_m^2)$.

In the absence of modulation ($\delta_m = 0$), the basic heat conduction state ($u = 0$) becomes unstable at $R = R_c \approx 1707.8$ against periodic convection-roll solutions with wavevector $q_c$. The orientation of $q_c$ is arbitrary, and its modulus is given as $|q_c| = 3.117$. In distinct contrast, all solutions of the OBE (2.6) for non-zero $\delta_m$ carry flow even for $R \propto \Delta T < 0$ (heating from above). So, we find convection rolls with modulation wavevector $q_m = (q_m, 0)$ for all finite $R$. It should be stressed that in contrast to standard RBC, the up–down symmetry ('Boussinesq symmetry') with respect to reflections at the midplane of the layer is broken by the temperature modulation.

For the analysis of the basic equations (2.6), we have employed some reformulations, in particular to get rid of the pressure $\Pi$. For the solenoidal vector field $u$, we use the general representation

$$u = \nabla \times (\nabla f \times e_z) + \nabla \Phi \times e_z \equiv \zeta f + \chi \Phi, \tag{2.7}$$

where the scalar functions $f(x, z)$ and $\Phi(x, z)$ describe the poloidal and toroidal components of $u$. The equations for $f$ and $\Phi$ are obtained by operating with the differential operators $\zeta$ and $\chi$ on (2.6b). Thus, we obtain from (2.6) our final set of equations:

$$\frac{\partial}{\partial t}\theta + (u \cdot \nabla)\theta + \delta_m R(u \cdot \nabla)\, T_m(x, z) = \nabla^2 \theta + R\Delta_2 f, \tag{2.8a}$$

$$\frac{1}{Pr}\left(\frac{\partial}{\partial t}\nabla^2 \Delta_2 f + \zeta \cdot [(u \cdot \nabla)u]\right) = \nabla^4 \Delta_2 f - \Delta_2 \theta - \delta_m R \Delta_2 T_m(x, z), \tag{2.8b}$$

$$\frac{1}{Pr}\left(\Delta_2 \frac{\partial}{\partial t}\Phi + \chi \cdot [(u \cdot \nabla)u]\right) = \nabla^2 \Delta_2 \Phi, \tag{2.8c}$$

where $\Delta_2 = \partial_{xx} + \partial_{yy}$ denotes the two-dimensional Laplacian; $\boldsymbol{u}$ has to be expressed in terms of the velocity functions according to (2.7). Note that the large-scale variations of $\varPhi$ in the plane describe a mean flow, which is crucial for the understanding of spiral defect chaos (see e.g. Chiam *et al.* 2003). Equations (2.8) are supplemented by the following boundary conditions:

$$\theta(\boldsymbol{x}, z = \pm 1/2) = f(\boldsymbol{x}, z = \pm 1/2) = \partial_z f(\boldsymbol{x}, z = \pm 1/2) = \varPhi(\boldsymbol{x}, z = \pm 1/2) = 0,$$
(2.9)

i.e. we assume realistic no-slip boundary conditions for $\boldsymbol{u}$.

The main issue of the present paper is the calculation of the forced roll solutions and the detailed analysis of their linear stability for moderate $R$ and not too large $\delta_m$. Some details of the mathematical methods to solve (2.8) are sketched in the following subsection.

## 2.2. *Calculation of forced roll solutions and their stability*

To condense the notation we introduce the symbolic vector $\widehat{\boldsymbol{V}} = (\theta, f, \varPhi)$ and rewrite (2.8) in a compact manner as follows:

$$\widehat{\mathscr{C}}(\partial_{\boldsymbol{x}}, \partial_z) \frac{\partial}{\partial t} \widehat{\boldsymbol{V}}(\boldsymbol{x}, z, t) + \widehat{\boldsymbol{N}}[\widehat{\boldsymbol{V}}, \widehat{\boldsymbol{V}}] + \delta_m R \widehat{\boldsymbol{N}}_m[\widehat{\boldsymbol{V}}, T_m]$$
$$= \widehat{\mathscr{L}}(\partial_{\boldsymbol{x}}, \partial_z; R) \widehat{\boldsymbol{V}}(\boldsymbol{x}, z, t) + \delta_m R \widehat{\boldsymbol{I}}[T_m]. \quad (2.10)$$

The explicit form of the linear operators $\widehat{\mathscr{C}}, \widehat{\mathscr{L}}$ is obvious by comparison with (2.8); this also applies to the nonlinearity $\widehat{\boldsymbol{N}}$, which is a bilinear differential operator with respect to $\widehat{\boldsymbol{V}}$. In comparison to non-modulated RBC, we have a new operator $\widehat{\boldsymbol{N}}_m[\widehat{\boldsymbol{V}}, T_m]$, which has only a $\theta$-component and an additive inhomogeneity $\delta_m R \widehat{\boldsymbol{I}}[T_m]$, only with an $f$-component.

Our analysis is restricted to large-aspect-ratio RBC ($L \gg d$), where periodic lateral boundary conditions are appropriate for solving (2.10). Thus, $\widehat{\boldsymbol{V}}$ is represented as a two-dimensional Fourier series in $\boldsymbol{x}$,

$$\widehat{\boldsymbol{V}}(\boldsymbol{x}, z, t) = \sum_{\boldsymbol{q}} \mathrm{e}^{\mathrm{i}\boldsymbol{q}\cdot\boldsymbol{x}} \boldsymbol{V}(\boldsymbol{q}, z, t), \quad (2.11)$$

where the condition $\boldsymbol{V}^*(\boldsymbol{q}, z, t) = \boldsymbol{V}(-\boldsymbol{q}, z, t)$ guarantees the reality of $\widehat{\boldsymbol{V}}$. In the following, a 'hat' as superscript will denote quantities in position space ($\boldsymbol{x}$), while the hat is suppressed for their counterparts in Fourier space ($\boldsymbol{q}$).

Let us start with the *unforced case* ($\delta_m = 0$), where the system (2.10) always allows for the trivial heat-conduction solution $\widehat{\boldsymbol{V}} = 0$ with $\theta = \boldsymbol{u} \equiv 0$. Linearization of (2.10) about $\widehat{\boldsymbol{V}} = 0$ thus leads to the following eigenvalue problem:

$$\sigma \mathscr{C}(\boldsymbol{q}, \partial_z) \boldsymbol{U}(\boldsymbol{q}, z; R) = \mathscr{L}(\boldsymbol{q}, \partial_z; R) \boldsymbol{U}(\boldsymbol{q}, z; R). \quad (2.12)$$

Here, we have switched in (2.10) to Fourier space by using the ansatz $\widehat{\boldsymbol{V}} = \mathrm{e}^{\sigma t} \mathrm{e}^{\mathrm{i}\boldsymbol{q}\cdot\boldsymbol{x}} \boldsymbol{U}(\boldsymbol{q}, z; R)$ for the eigenmodes. The operators $\mathscr{C}, \mathscr{L}$ in (2.12) derive from $\widehat{\mathscr{C}}, \widehat{\mathscr{L}}$ in (2.10), respectively, by the substitution $\partial_{\boldsymbol{x}} \to \mathrm{i}\boldsymbol{q}$. The discrete set of eigenvalues $\sigma = \sigma_i(\boldsymbol{q}, R)$, $i = 0, 1, 2, \ldots$, of the Liouville-type eigenvalue problem (2.12) is ordered in decreasing order with respect to their real parts: $\mathrm{Re}\,\sigma_0 \geqslant \mathrm{Re}\,\sigma_1 \geqslant \mathrm{Re}\,\sigma_2, \ldots$. Note that $\sigma_i$ and the corresponding eigenvectors $\boldsymbol{U}_i$ only depend on $|\boldsymbol{q}| = q$ and that

in general $\mathrm{Im}[\sigma_0(q, R)] = 0$ for the present system. The vanishing growth rate, $\mathrm{Re}[\sigma_0(q, R)] = 0$, defines the familiar *neutral curve* $R = R_0(q)$ for non-modulated RBC: for $R > R_0(q)$, the heat-conduction state is unstable to convection. The minimum of $R_0(q)$ at the critical wavenumber $q_c$ yields the threshold $R_c = R_0(q_c)$.

For $\delta_m \neq 0$ we first concentrate on stationary roll solutions, $\widehat{V}_r(\boldsymbol{x}, z; q_m, R)$ of (2.10), which are locked to the external wavevector $\boldsymbol{q}_m = (q_m, 0)$. In line with (2.11), we start with the ansatz

$$\widehat{V}_r(\boldsymbol{x}, z; q_m, R) = \sum_{\boldsymbol{q} \in \boldsymbol{Q}_m} \mathrm{e}^{\mathrm{i}\boldsymbol{q}\cdot\boldsymbol{x}} V_r(\boldsymbol{q}, z; R), \tag{2.13}$$

where $\boldsymbol{Q}_m = \{(k\, q_m, 0)\}_{k=-N,\dots,N}$, i.e. the wavevectors $\boldsymbol{q}$ are restricted to the finite grid $\boldsymbol{Q}_m$ with $2N + 1$ members.

In this paper, the $z$-dependence of all quantities like $\widehat{V}_r(\boldsymbol{x}, z; q_m, R)$ (2.13) is captured by standard Galerkin methods. They involve expansions in terms of suitable orthogonal functions, which satisfy the required boundary conditions (2.9) at the confining plates. For $\theta$ and $\Phi$ we use the trigonometric functions $S_n(z) = \sin(n\pi(z + 1/2))$, with $S_n(\pm 1/2) = 0$, and for $f$ the Chandrasekhar functions $C_n(z)$ (as defined in Chandrasekhar 1961), where $1 \leqslant n \leqslant M$.

Introducing the Fourier expansion $\widehat{V}_r$ (2.13) into (2.8) and projecting onto the Galerkin functions results in a system of $3M(2N + 1)$ coupled nonlinear algebraic equations for the corresponding expansion coefficients. This system is solved using a Newton–Raphson iteration scheme. We have tested that extending the summations in (2.13) beyond the truncation parameters, $N = 10$ and $M = 8$, respectively, leads to negligible changes of the roll solutions.

To investigate the linear stability of the forced roll $\widehat{V}_r$ (2.13) with respect to small perturbations $\delta\widehat{V}(\boldsymbol{x}, z, t)$, we use the standard Floquet ansatz:

$$\delta\widehat{V}(\boldsymbol{x}, z, t) = \mathrm{e}^{\Lambda t}\, \mathrm{e}^{\mathrm{i}\boldsymbol{s}'\cdot\boldsymbol{x}} \sum_{\boldsymbol{q} \in \boldsymbol{Q}_m} \mathrm{e}^{\mathrm{i}\boldsymbol{q}\cdot\boldsymbol{x}} \delta V(\boldsymbol{q}, z). \tag{2.14}$$

Linearization of (2.10) with respect to $\delta\widehat{V}$ results in a linear eigenvalue problem of dimension $3M(2N + 1)$ for the 'vector' of all the expansion coefficients. Standard linear algebra packages (LAPACK) are used to determine the set of eigenvalues $\Lambda$ and the corresponding eigenvectors $\delta\widehat{V}$, defined in (2.14), which depend on $\boldsymbol{s}'$ and $R, Pr, q_m$ and $\delta_m$. Among all the eigenvalues $\Lambda$, we are mainly interested in the one with the largest real (Re) part, $\Lambda_0(\boldsymbol{s}')$, which defines the growth rate $\lambda_0(\boldsymbol{s}') \equiv \mathrm{Re}[\Lambda_0(\boldsymbol{s}')]$. We then have to determine the maximum, $\lambda_{max}(R, q_m, Pr, \delta_m)$, of $\lambda_0(\boldsymbol{s}')$ with respect to the Floquet vector $\boldsymbol{s}'$. Zeros of $\lambda_{max}$ signal linear instabilities of the periodic roll solution in the $R$–$q_m$ plane for fixed $Pr$ and $\delta_m$.

To study more complex patterns and validate the Galerkin solutions direct simulations of the OBE (2.8) have been performed. The numerical solutions have been obtained by slightly generalizing our well-proved solver for standard Rayleigh–Bénard convection (see e.g. Pesch 1996) and §3.4 in Bodenschatz *et al.* (2000). The code makes use of Galerkin expansions with respect to the $z$-dependence and treats the $\boldsymbol{x}$-dependence in Fourier space via a pseudo-spectral technique. The time stepping is performed by a semi-implicit Adams–Bashforth scheme. By using a small ($M \leqslant 8$) but sufficient number of modes in the $z$-direction, the computational time becomes small enough to allow simulations of fairly large aspect ratio systems. We conducted simulations based on up to $256 \times 256$ grid points in Fourier space, corresponding to an area of approximately $20\lambda_m \times 20\lambda_m$ in real space, with $\lambda_m = 2\pi/q_m$.
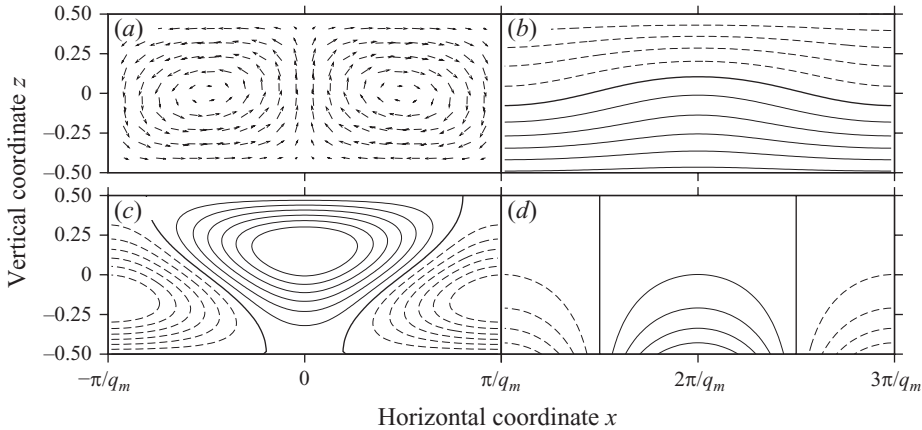
FIGURE 1. Forced roll solution in the $x$–$z$ plane for the parameters $q_m = q_c$, $\delta_m = 0.01$, $Pr = 1$ and $\epsilon = (R - R_c)/R_c = 0.2$. (*a*) Velocity field $\boldsymbol{u}$; (*b*) isolines of the temperature $T(x, z)$ (2.3*a*) after subtracting the reduced mean temperature $\bar{T}R/\Delta T$ in (2.3*b*); (*c*) isolines of the 'convective' temperature contribution $\theta(x, z)$ (2.3*a*); (*d*) isolines of $T_m(x, z)$ originating from the modulated boundary condition, see (2.4). Dashed isolines indicate negative values of the corresponding fields.

## 3. The forced roll solution

In this section we will briefly sketch the $q_m$-periodic roll solutions (2.13) of (2.8). Here and in the following, we will concentrate mainly on the parameters covered in the recent experiments, where $q_m \approx q_c$, $\delta_m \approx 0.01$ and $Pr \approx 1$. Instead of the Rayleigh number $R$, often the reduced distance $\epsilon = (R - R_c)/R_c$ from the critical Rayleigh number $R_c$ for $\delta_m = 0$ is used. The roll solutions are governed by the fields $\theta$ and $f$, while $\Phi \equiv 0$. As already mentioned, the presence of modulation ($\delta_m \neq 0$) prohibits non-convective solutions ($\boldsymbol{u} = 0$) of the OBE for finite $R$.

For small $R \ll R_c$, the functions $\theta$, $f$ vary as $\cos(q_m x)$ in the $x$-plane with an amplitude proportional to $\delta_m$. With increasing $R$, nonlinear corrections in the form of higher harmonics come into play.

In figure 1 we show a representative forced roll solution of (2.8) for $R = 1.2R_c$. We have perfect agreement of the Galerkin solution with the corresponding numerical solution of the OBE starting from random initial conditions. The external temperature modulation $T_m$ (2.4), shown in figure 1(*d*), has maxima at $x = 0, \pm 2\pi/q_m, \dots$, and breaks the translational symmetry. Thus, the positions of the rolls along the $x$-axis are locked and we have maximal up-flow at the maxima of $T_m$ (as shown in figure 1*a*). The numerical values of the fields $\theta$ and $f$ are very close to the corresponding ones for $\delta_m = 0$. Decreasing $R$ leads to qualitatively similar convection rolls except that their centres move slightly towards $z = -1/2$.

Convection patterns are typically visualized in experiments by the shadowgraph method. According to Trainoff & Cannell (2002), the shadowgraph intensity is governed by the vertical ($z$) average $T_v(\boldsymbol{x}) = \langle T(\boldsymbol{x}, z) \rangle$ of the whole temperature field (2.3*a*). In the case of forced rolls we thus arrive at the following Fourier series:

$$T_v(\boldsymbol{x}) = t_0 + t_1 \cos(q_m x) + t_2 \cos(2q_m x) + \cdots . \tag{3.1}$$

The 'shadowgraph amplitude' $t_1$ serves as our global measure of the roll amplitudes. According to (2.3) it splits into a 'quasi-conductive' part, $\langle t_m \rangle$, originating from $T_m(\boldsymbol{x}, z)$
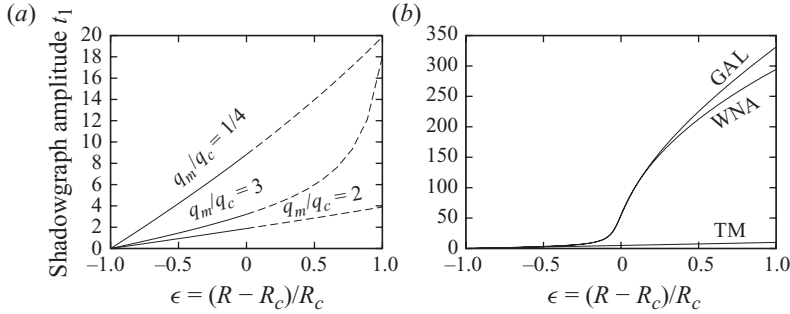
FIGURE 2. Shadowgraph amplitude $t_1$ (3.1) of forced roll solutions as a function of $\epsilon$ for $Pr = 1$ and $\delta_m = 0.01$. When the lines become dashed the rolls are linearly unstable (see §4). (a) Non-resonant case ($q_m \neq q_c$) and (b) resonant case ($q_m = q_c$). Here, we have also included the weakly nonlinear approximation (WNA) of $t_1$ (see text). The small 'quasi-conductive' contribution $\langle t_m \rangle$ (TM) is practically not relevant.

and a 'convective' part, $t_\theta$, from $\theta(x, z)$. In figure 2, we show $t_1$ as a function of $\epsilon$ for different values of $q_m$ and for a representative small modulation amplitude $\delta_m = 0.01$. The shape of the curves depends sensitively on the ratio $q_m/q_c$. In the vicinity of $\epsilon = -1$, i.e. for small $R \propto \Delta T$, the shadowgraph amplitude $t_1$ reflects the linearity of $\langle t_m \rangle \propto \delta_m R$ with respect to $\epsilon$ and $\delta_m$. When, however, $R \gtrsim R_0(q_m)$, with $R_0(q_m)$ being the neutral curve of non-modulated RBC (see after (2.12)), significant deviations from the linear behaviour develop. This is in particular demonstrated in figure 2(b) for $q_m = q_c$. In fact, at $R = R_0(q_m) = R_c$, i.e. at $\epsilon = 0$, one observes a strong increase of $t_1$ for which $t_\theta$ is responsible.

For a better understanding of the $t_\theta$ contribution to $t_1$ in figure 2, the weakly nonlinear approximation scheme is very useful. To construct the forced roll solution of (2.10) we start in the spirit of Cross (1980) from the following ansatz for $\widehat{V}(x, z, t)$ (2.13):

$$\widehat{V}(x, z, t) = F(t) \, e^{iq_m \cdot x} U_0(q_m, z; R) + \text{c.c.}, \tag{3.2}$$

with $U_0(q_m, z; R)$ as the eigenmode for the maximal eigenvalue $\sigma_0(q, R)$ in (2.12). In the regime $q_m \approx q_c$ and $R \approx R_c$, we have

$$\sigma_0(q_m, R) = \frac{1}{\tau_0} \frac{R - R_0(q_m)}{R_c}, \tag{3.3}$$

where $\tau_0^{-1} = 19.65 \, Pr/(Pr + 0.5177)$ denotes the familiar relaxation time. The neutral curve, $R_0(q)$, can be approximated near $q_c$ by

$$R_0(q) = R_c \left[ 1 + \frac{\xi_0^2}{4q_c^2} (q^2 - q_c^2)^2 \right], \tag{3.4}$$

with the correlation length $\xi_0^2 = 0.148$ (Cross & Hohenberg 1993). A systematic expansion with respect to the amplitude $F$ in (2.10) in the limit $\delta_m \to 0$ leads to the amplitude equation

$$\tau_0 \partial_t F(t) = \left[ \epsilon - \frac{\xi_0^2}{4q_c^2} (q_m^2 - q_c^2)^2 \right] F - g_0 F |F^2| + \delta_m g_2, \tag{3.5}$$

where forcing has only led to an additive correction $\propto \delta_m$ of the standard amplitude equation for RBC in the absence of forcing (see e.g. Cross 1980). Note that a

correct balancing of all terms in (3.5) with respect to $\delta_m$ requires $F \sim \delta_m^{1/3}$ and $|q_m - q_c|^2 \sim \epsilon \sim \delta_m^{2/3}$. The amplitude equation (3.5) has been derived more systematically by using a double expansion with respect to the small parameters $\epsilon$ and $\delta_m$ by Vozovoi & Nepomnyashchy (1974) and more comprehensively by Kelly & Pal (1978). Only one of the three stationary solutions of (3.5) is stable and thus relevant; it can be chosen real and reads as

$$F_0(q_m, \epsilon) = \left( \frac{\delta_m g_2}{2 g_0} \right)^{1/3} \left( \frac{\tilde{\epsilon}}{f(\tilde{\epsilon})} + f(\tilde{\epsilon}) \right), \tag{3.6a}$$

with

$$\tilde{\epsilon} = \frac{2}{3} \left( 2 \delta_m^2 g_2^2 g_0 \right)^{-1/3} \left[ \epsilon - \frac{\xi_0^2}{4 q_c^2} (q_m^2 - q_c^2)^2 \right] \tag{3.6b}$$

and

$$f(\tilde{\epsilon}) = (1 + \sqrt{1 - \tilde{\epsilon}^3})^{1/3}. \tag{3.6c}$$

This solution describes the 'imperfect' bifurcation in the presence of forcing in figure 2(b): in the limit $\delta_m \to 0$, one obtains from (3.6a–c)

$$F_0 = \left[ \left( \epsilon - \frac{\xi_0^2}{4 q_c^2} (q_m^2 - q_c^2)^2 \right) \Big/ g_0 \right]^{1/2}, \tag{3.7}$$

which contains the bifurcation of convection from the basic state $F_0 = 0$ at the neutral curve $\epsilon = (\xi_0^2 / 4 q_c^2)(q_m^2 - q_c^2)^2$. For finite $\delta_m$, however, this bifurcation is smoothed out and the amplitude takes the finite value $F_0 = (\delta_m g_2 / g_0)^{1/3}$ at the neutral curve. The actual values of the coefficients $g_0$ and $g_2$ in (3.5) depend on the normalization of the eigenvector $U_0 \equiv (f_0, \theta_0, 0)$ (2.12) used in (3.2). Following the familiar convention $2 \langle f_0 \theta_0 \rangle = R_c / q_c^2$ (Cross & Hohenberg 1993), we arrive at the following coefficients in (3.5):

$$g_0 = 0.6995 - 0.0047 \, Pr^{-1} + 0.0083 \, Pr^{-2}, \quad g_2 = 0.633, \tag{3.8}$$

for further details we refer to the Appendix (see (A 8) and (A 9)). Our results are consistent with those of Kelly & Pal (1978), where a different normalization of the eigenvector $U_0$ was chosen.

The temperature component of $\widehat{V}$ (3.2) with $F_0$ from (3.6a–c) determines the convective contribution $t_\theta$ (see after (3.1)) to the shadowgraph amplitude $t_1$ in the weakly nonlinear approximation (WNA). As demonstrated in figure 2(b), one finds excellent agreement with the exact Galerkin result (GAL) in the vicinity of $\epsilon = 0$ (see also Seiden *et al.* 2008).

For the special case $q_m = q_c/2$, however, the amplitude $t_2$ of the Fourier mode $\cos(2 q_m x)$ in (3.1) becomes considerably larger than $t_1$, when $R$ exceeds $R_c$. This is clearly visible in figure 3. The increasing prevalence of $t_2$ for $R \gtrsim R_c$ can be explained by a resonant coupling of the higher harmonic modes $\propto \cos(2 q_m x)$ in the forced rolls to the critical mode of unforced RBC at $R \approx R_c$ with the wavenumber $q_c = 2 q_m$ (see e.g. Hall & Walton 1978 and also Kelly 1993). Note that this mechanism requires a broken Boussinesq symmetry, as in our case, otherwise it would be prohibited by the opposite $z$-symmetry of the two modes.

## 4. Stability of forced solutions: Galerkin approach

In the following, we analyse the stability of the forced roll solutions in the $\epsilon$–$q_m$ plane on the basis of the calculational scheme given in §2. A representative stability
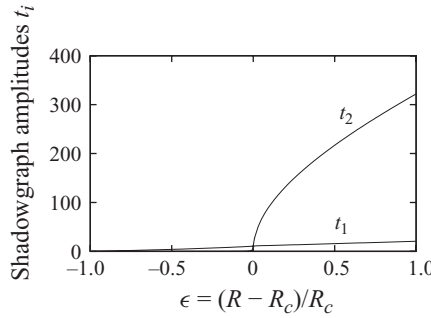
FIGURE 3. Fourier coefficients $t_1$ and $t_2$ of the shadowgraph expansion (3.1) for $q_m/q_c = 1/2$, $Pr = 1$ and $\delta_m = 0.01$. Note that $t_2$ is a measure of the $q_c$-contribution.
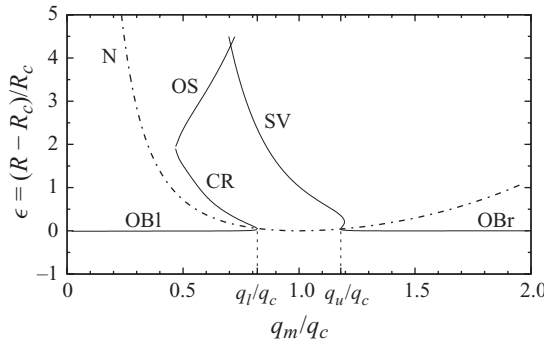


FIGURE 4. Stability diagram of the forced roll solution for $Pr = 1$ and $\delta_m = 0.01$ with the dash-dotted neutral curve (N). Note the 'gap of instability' ($q_l \leqslant q_m \leqslant q_u$) for $q_m \approx q_c$, where the stability domain extends up to fairly large $\epsilon$. For details of the different types of destabilization (OBl, OBr, CR, OS and SV), see text.

diagram for the parameters $\delta_m = 0.01$ and $Pr = 1$, which corresponds to the recent experiments (McCoy *et al.* 2008; Seiden *et al.* 2008), is shown in figure 4. The boundary of the stability regime of the forced rolls, which are stable for $R < R_c$, is delineated by solid lines: it consists of different parts marked by capital letters OBl, CR, OS, SV and OBr, which denote different destabilization mechanisms. In view of (2.14), they are characterized by the wavevector $\boldsymbol{s} = \boldsymbol{s}' + \boldsymbol{q}_{max}$ of the dominant destabilizing mode, where $\boldsymbol{q}_{max} \in \boldsymbol{Q}_m$ (2.13) denotes the maximum of $\delta V(\boldsymbol{q}, z)$ with respect to $\boldsymbol{q}$ and $\boldsymbol{s}'$ denotes the corresponding Floquet wavevector.

Inspection of figure 4 immediately shows with OBl ($q_m < q_l$) and OBr ($q_m > q_u$) two regimes, where the instability limits practically coincide with the horizontal line $\epsilon = 0$. In the intervening wedge-like region bounded by the lines CR, OS and SV, stable forced rolls exist for larger $\epsilon$.

### 4.1. *Oblique-roll instability*

Along the instability lines marked with OBl and OBr in figure 4, the forced rolls are found to be most unstable to a pair of degenerate *oblique* modes with wavevectors $\boldsymbol{s}_{1,2}$ of modulus $s_1 = s_2 = q_c$ which form together with $\boldsymbol{q}_m$ a resonant triad:

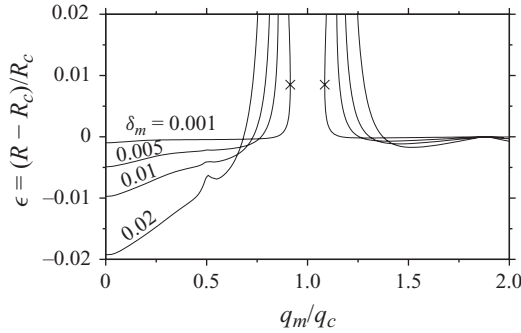$$\boldsymbol{q}_m = \boldsymbol{s}_1 + \boldsymbol{s}_2, \tag{4.1}$$

FIGURE 5. Enlarged view of the instability limits OBl and OBr of figure 4 in the $\epsilon$–$q_m$ plane for different values of $\delta_m$ (for details, see text). Note that the $\epsilon$-scale ($O(10^{-2})$) is significantly smaller than that in figure 4. The turning points for $\delta_m = 0.001$ have been marked.
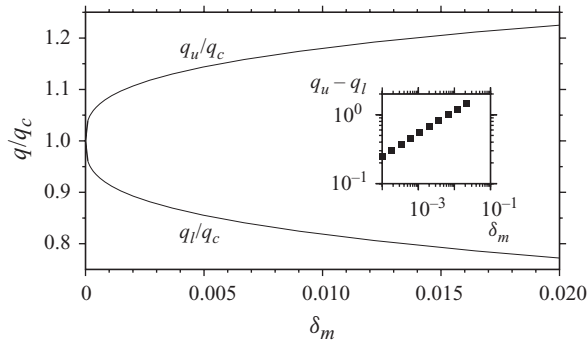


FIGURE 6. The lower ($q_l$) and the upper turning points ($q_u$) of the instability curves $\epsilon_{ob}(q_m/q_c)$ in figure 4 for $Pr = 1$ as a function of modulation amplitude $\delta_m$; inset: gap of instability for small $\delta_m$ (double-logarithmic scale).

where $s_{1,2} = (q_m/2, \pm\sqrt{q_c^2 - q_m^2/4})$. This destabilization mechanism has first been identified in the approximate calculations by Vozovoi & Nepomnyashchy (1974) and later by Pal & Kelly (1979).

In figure 5, we present for different $\delta_m$ the oblique-roll instability curves $\epsilon = \epsilon_{ob}(q_m/q_c)$ in much higher resolution in $\epsilon$ than in figure 4. It is evident that the instability appears in general at Rayleigh numbers $R = R_{ob} < R_c$, i.e. at $\epsilon_{ob} = (R_{ob} - R_c)/R_c < 0$. Starting at fixed $\delta_m$ with small $q_m$, the function $\epsilon_{ob}(q_m/q_c)$ rises with increasing $q_m$, crosses $\epsilon = 0$, where the slope gets large, and bends back at a lower turning point $q_m = q_l < q_c$ towards smaller $q_m$; a corresponding upper turning point exists at $q_m = q_u > q_c$ on the right side of figure 4. The values of $q_u$ and $q_l$, which determine the 'gap of instability' in figure 4, are shown in figure 6 as a function of $\delta_m$. The scaling law $q_u - q_l \propto \delta_m^{1/3}$ (see inset) will become clear in the framework of amplitude equations in §5, where the impact of possibly competing destabilization mechanisms will also be explored. According to figure 5 the widening of the instability gap as a function of $\delta_m$ is also accompanied by a decrease of the ordinates of $\epsilon_{ob}(q_m/q_c)$ roughly proportional to $\delta_m$. The hump at $q_m/q_c = 1/2$, which becomes more pronounced with increasing $\delta_m$, is due to the resonant interaction with $q_c$-modes reflected also in the large amplitude $t_2$ in figure 3 for $R \gtrsim R_c$.
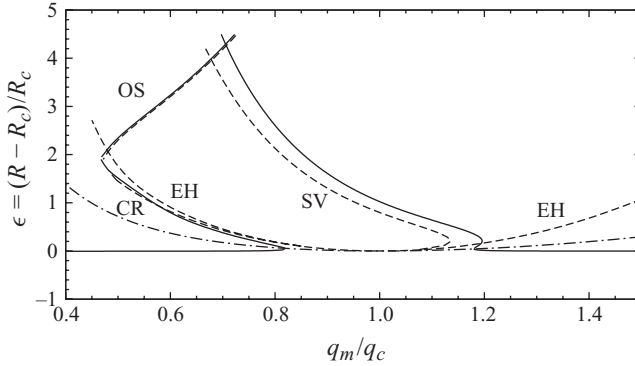
FIGURE 7. Copy of the central region ($q_m \approx q_c$) of the stability diagram in figure 4 (solid lines) for $\delta_m = 0.01$ compared to the standard Busse balloon for $\delta_m = 0$ (dashed lines). The cross-roll (CR) and oscillatory (OS) instabilities practically coincide, while the skewed-varicose (SV) instability boundary has moved up in $\epsilon$ by a relatively constant offset. The Eckhaus (EH) instability has no direct counterpart at finite $\delta_m$. The neutral curve (dash-dotted) is included as well.

For $q_m/q_c < 0.15$, our numerical methods become more and more unreliable: in this regime, the Fourier series (2.14) converges poorly, due to the higher harmonic contributions in $\delta\widehat{V}(\boldsymbol{x}, z, t)$. Within our numerical accuracy, a non-resonant destabilization against pure transverse rolls with wavevector $\boldsymbol{s}_t = (0, q_c)$ is practically indistinguishable from the resonant one to oblique rolls. It cannot be ruled out that the transverse destabilization might prevail at very small $q_m/q_c$, as suggested in Pal & Kelly (1979) in the limit $\delta_m \rightarrow 0$. That analysis, however, was restricted to the small cutoff $N = 1$ (2.13) in Fourier space, which is certainly insufficient for small $q_m$.

Let us now switch to the case $q_m > q_c$ in figure 5, where according to (4.1) the oblique-roll instability is confined to the interval $q_u < q_m < 2q_c$. Except that the ordinates $\epsilon_{ob}(q_m/q_c)$ of the OBr–curve are considerably smaller in magnitude than for $q_m < q_l$, there is in principle not much difference to the case $q_m < q_u$ (curve OBl).

The stability of the forced rolls for $q_m \gtrsim 2q_c$ has not been examined systematically in the framework of the Galerkin analysis. Here we sketch only some results exclusively for $\delta_m = 0.01$ and $Pr = 1$. In the interval $2q_c \lesssim q_m \lesssim 2.08q_c$, we find a continuous bifurcation to longitudinal rolls with wavevector $\boldsymbol{s} = (q_c, 0)$ at a slightly negative $\epsilon$. Passing $q_m/q_c \approx 2.08$, a bifurcation to transverse modes with wavevector $\boldsymbol{s}_t = (0, q_c)$ takes over, which appears at negative though extremely small values $\epsilon_t = (R_t - R_c)/R_c$ of the order of $10^{-4}$. Additional information is postponed to §6.2, where we will also comment on the special case $q_m/q_c = 3$.

## 4.2. *Stability of rolls for $q_m \approx q_c$*

We now turn our attention to the wedge-like region of the stability diagram around $q_m/q_c \approx 1$ in figure 4, which has been redrawn in figure 7 in comparison to the familiar Busse balloon for $\delta_m = 0$. The regime of stable forced rolls is confined on the left by the stationary cross-roll (CR) instability, where the wavevector $\boldsymbol{s}$ of the destabilizing mode is perpendicular to $\boldsymbol{q}_m$ with $s \approx q_c$. From above, it is limited by an oscillatory instability (OS), which has been first analysed by Clever & Busse (1974) for $\delta_m = 0$. It is characterized by a transverse travelling-wave mode with wavevector $\boldsymbol{s} = (0, q_c)$ and exists at medium and small $Pr$. It is plausible that for larger $\epsilon$, where the forced roll

solution approaches more and more the unforced one, the CR and the OS instability lines for small $\delta_m \neq 0$ follow those for $\delta_m = 0$ quite well.

On the right-hand side of the wedge region, the instability line of the forced rolls is governed by modes with wavevectors $s$, which can be written as

$$s = q_m - s', \qquad (4.2)$$

where $s' = s'(\cos\phi, \sin\phi)$. In line with the discussion in §2.2 (see after (2.14)), the instability limit is characterized by the vanishing growth rate $\lambda_0(R, q_m, s')$ of linear perturbations of the forced rolls, where $\lambda_0(s')$ has to be evaluated at its maximum $s'_{max} = s'_{max}(\cos\phi_{max}, \sin\phi_{max})$. For unforced RBC ($\delta_m = 0$), one thus obtains the common long-wavelength skewed-varicose (SV) instability (figure 7), where $s'_{max} \to 0$. It grows out of the marginal translational mode, which is known to be closely related to translation invariance. The angle $\phi_{max}$ decreases roughly from $40°$ to $30°$ with increasing $\epsilon$ for $Pr = 1$. For $q_m = q_c$, one finds for instance $\phi_0 \equiv \phi_{max} = 38.8°$. Because of the stabilizing effect of forcing, the instability curve for $\delta_m > 0$ has generically to move upwards to larger $\epsilon$ as shown in figure 7. The upward shift is in fact roughly constant in the $\epsilon$–$q_m$ plane and was found to be approximately proportional to $\delta_m$. The angle $\phi_{max}$, however, which characterizes the Floquet exponent $s'$ (4.2), turns out to be practically $\delta_m$-independent, while in the absence of translational invariance, $s'_{max}$ had to move continuously away from its value $s'_{max} = 0$ for $\delta_m = 0$.

Note that in the unforced case ($\delta_m = 0$) the Busse balloon is limited at small $\epsilon$ and for $q \gtrsim q_c$ from below by the long-wavelength Eckhaus instability with $s' \to 0$ and $\phi_{max} = 0$ in (4.2). For $q \lesssim q_c$ the long-wavelength zigzag instability, where $\phi_{max} = 90°$, competes with the Eckhaus instability. In analogy to the discussion before, these instabilities should be partially suppressed at finite $\delta_m$ in the absence of translational invariance. To which extent they then compete with the oblique-roll instability will be discussed in §5.

## 5. Stability of forced rolls: amplitude-equation approach

In this section, we will support our results of §4 on the Busse balloon of forced rolls by suitable amplitude equations. In this way, we arrive in particular at analytical expressions for the various stability limits. Our analysis has profited to some extent from the ideas of Vozovoi & Nepomnyashchy (1974). A direct comparison with their explicit results is not possible, since their calculations were based on the use of (non-realistic) free-slip boundary conditions in RBC.

### 5.1. *Oblique-roll instability for $q_m \approx q_c$*

As discussed before, the oblique-roll instability of the forced roll solution $\widehat{V}_r$ (2.13) is driven by two degenerate modes with wavevectors $s_{1,2}$ ($s_i = q_c$), as defined in (4.1), which include the angle $\beta = \arccos(q_m/(2q_c))$ with $q_m$. We represent the corresponding perturbation

$$\delta\widehat{V}_{ob}(x, z, t) = A_1(t)\, e^{is_1 \cdot x} U_0(s_1, z; R_c) + A_2(t)\, e^{is_2 \cdot x} U_0(s_2, z; R_c) + \text{c.c.} \qquad (5.1)$$

in terms of the eigenfunctions $U_0$ (2.12) and linearize (2.10) about $\widehat{V}_r$. Along the instability limits OBl and OBr, where $\epsilon = (R - R_c)/R_c \approx 0$, we arrive to leading order in $\delta_m$ at the following generic system of two coupled amplitude equations:

$$\tau_0 \partial_t A_1 = (\epsilon + \Delta_\epsilon)A_1 + \delta_m \eta A_2^* - g_0 A_1 |A_1|^2 - g_0 \gamma' A_1 |A_2|^2, \qquad (5.2a)$$

$$\tau_0 \partial_t A_2 = (\epsilon + \Delta_\epsilon)A_2 + \delta_m \eta A_1^* - g_0 A_2 |A_2|^2 - g_0 \gamma' A_2 |A_1|^2. \qquad (5.2b)$$

The calculation of the 'linear' coefficients $\eta$ (see (A 10)) and $\Delta_\epsilon$ (see (A 13)) as a function of $q_m/q_c$ is sketched in the Appendix. Here also, the cross-coefficient $\gamma' = \gamma(\beta')$ is discussed, with $\beta' = 2\beta$ (A 8); for the cubic coefficient $g_0$ see (3.8). Note that coupled amplitude equations of the same structure have already appeared in the literature (Zimmermann *et al.* 1993; Manor, Hagberg & Meron 2008, 2009) in the context of models describing a multiplicative forcing via the control parameter $\epsilon$. The analysis in these papers can be closely followed after a suitable re-definition of the coefficients. The ansatz $A_i(t) = a_i \, \mathrm{e}^{\sigma t}$ in (5.2a,b) leads to the growth rate $\sigma = (\epsilon + \Delta_\epsilon + \delta_m |\eta|)/\tau_0$ and thus from $\sigma = 0$ to the approximate instability limit $\epsilon_{ob}^A$:

$$\epsilon_{ob}^A = -\Delta_\epsilon - \delta_m |\eta|. \tag{5.3}$$

The coefficients $a_i$ can be chosen real with $a_2 = \mathrm{sgn}(\eta) a_1$. We have found that the Galerkin results for $\epsilon_{ob}$ in figure 5 are very well approximated by $\epsilon_{ob}^A$ along the curve OBr for $q_m > q_c$. For a representative example we refer to the discussion of figure 11 in §6.1, which deals with a numerical solution of the OBE for $q_m/q_c = 1.6$. In a similar way, the regime $0.55 q_c < q_m < q_l$ along OBl is well described by (5.3). For smaller $q_m$, this approximation does not work satisfactorily, since the coefficient $\Delta_\epsilon$ is poorly captured by the weakly nonlinear analysis.

In the vicinity of $q_m/q_c \approx 1$ we make use of the explicit expressions for $\eta$ (A 11) and for $\Delta_\epsilon$ (A 14) in the Appendix and thus arrive at an implicit equation

$$\epsilon_{ob}(Q) = \gamma_{ob} g_0 |F_0(Q, \epsilon_{ob}(Q))|^2 - \delta_m |\eta|, \tag{5.4}$$

for the instability curve $\epsilon_{ob}(Q)$, where $Q = q_m - q_c$ and $\gamma_{ob} \equiv \gamma(\beta)$ for $\beta = 60°$ (see (A 8)). The forced roll amplitude $F_0(Q, \epsilon)$ in (5.4), which is even in $Q$, derives from the amplitude equation (3.5) by expanding with respect to $Q$ up to second order:

$$0 = \left[\epsilon - \xi_0^2 Q^2\right] F_0(Q, \epsilon) - g_0 F_0^3 + \delta_m g_2. \tag{5.5}$$

The explicit solution $F_0(Q, \epsilon)$ can be obtained in analogy to (3.6a–c).

In figure 8, we show a representative graph of $\epsilon_{ob}(Q)$ for $Q < 0$, which agrees very well with the fully numerical Galerkin results. The condition $\mathrm{d}Q/\mathrm{d}\epsilon_{ob} = 0$ defines the two turning points, $(\pm Q_{ob}^{tp}, \epsilon_{ob}^{tp})$, of $\epsilon_{ob}(Q)$, which determine the gap of instability in figure 4. After some algebra we obtain in leading order in $\delta_m$ the following closed expressions:

$$Q_{ob}^{tp} = \frac{\sqrt{3}}{2^{1/3}\xi_0} \left((\gamma_{ob} - 1) g_0 g_2^2\right)^{1/6} \delta_m^{1/3}, \quad \epsilon_{ob}^{tp} = \epsilon_{ob}\left(Q_{ob}^{tp}\right) = \frac{(\xi_0)^2 \gamma_{ob}}{3(\gamma_{ob} - 1)} \left(Q_{ob}^{tp}\right)^2, \tag{5.6}$$

which yields $Q_{ob}^{tp} = 2.698 \, \delta_m^{1/3}$ and $\epsilon_{ob}^{tp} = 0.905 \, \delta_m^{2/3}$ for $Pr = 1$.

## 5.2. *Cross-roll instability*

In this section we briefly discuss the cross-roll instability limit, $\epsilon_{cr}(Q)$, which joins in figure 4 to the OBl line near the left turning point. The wavevector $s$ of the perturbing mode with modulus $q_c$ forms an angle of $90°$ with $q_m$ instead of $60°$ as in §5.1. Thus, only the symbols $\epsilon_{ob}$ and $\gamma_{obl}$ in (5.4) and (5.6) have to be replaced by $\epsilon_{cr}(Q)$ and $\gamma_{cr} \equiv \gamma(\beta = 90°)$, respectively. The resonance term $\propto \eta$ in (5.4) is absent. Thus in analogy to (5.6) we obtain the following implicit equation for $\epsilon_{cr}(Q)$:

$$\epsilon_{cr}(Q) = \gamma_{cr} g_0 |F_0(Q, \epsilon_{cr}(Q))|^2. \tag{5.7}$$
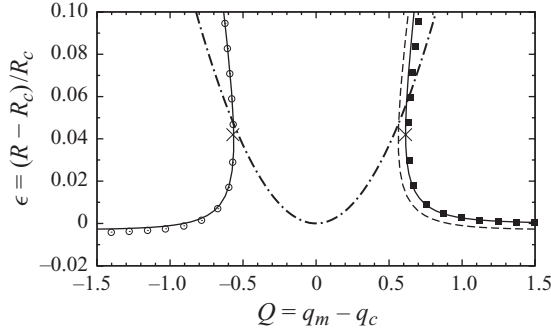
FIGURE 8. The oblique-roll instability curve $\epsilon_{ob}(|Q|)$ (5.4) for $Pr = 1$ and $\delta_m = 0.01$; solid line for $Q < 0$ and dashed for $Q > 0$. For $Q > 0$, the Eckhaus instability curve $\epsilon_E(Q)$ (solid line) from (5.10) is also shown. The corresponding turning points from (5.6) and (5.11), respectively, marked by crosses, are located near the crossings of the two curves with the neutral curve $\epsilon = \xi_0^2 Q^2$ of non-modulated RBC (dash-dotted). Open circles and filled squares, respectively, indicate the exact Galerkin results.
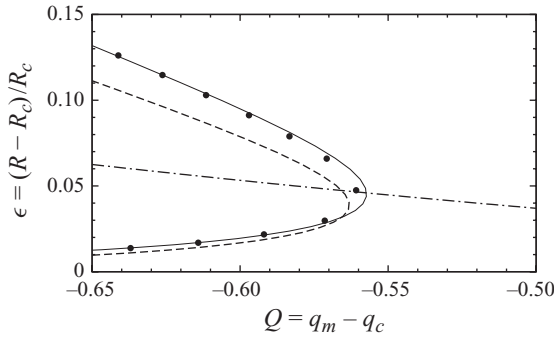


FIGURE 9. Cross-roll instability limit $\epsilon_{cr}(Q)$ (solid line) for $Pr = 1$ and $\delta_m = 0.01$ near $q_m/q_c = 1$ and $\epsilon = 0$ from (5.7) in comparison with the Galerkin results (filled circles). The oblique-roll instability line (dashed) $\epsilon_{ob}(Q)$ (see figure 8) and the neutral curve (dash-dotted) have been included as well.

Thus, $\epsilon_{cr}(Q)$ is even in $Q$; the coordinates of the turning points are obtained from (5.6) with the replacement $\gamma_{obl} \to \gamma_{cr}$. We thus obtain $Q_{cr}^{tp} = 2.587\,\delta_m^{1/3}$ and $\epsilon_{cr}^{tp} = 0.976\,\delta_m^{2/3}$ for $Pr = 1$. As evident in figure 9, the curve $\epsilon = \epsilon_{cr}(Q)$ matches well with the exact Galerkin values. In agreement with figure 7, the oblique-roll instability prevails at small $\epsilon$ in contrast to the converse situation at larger $\epsilon$ above the turning point.

### 5.3. *Eckhaus instability*

In the preceding sections, the oblique-roll and the cross-roll instabilities have been discussed for $q_m \approx q_c$. In non-modulated RBC ($\delta_m = 0$), one observes well-known long-wavelength instabilities (Eckhaus and zigzag) in this regime as well. To study the Eckhaus instability, which is characterized by slow modulations of the wavenumber of the rolls, we employ for the perturbing modes, in analogy to (5.1), the ansatz

$$\delta \widehat{V}_E(\boldsymbol{x}, z, t) = A_1(t)\,e^{isx}\,e^{i\boldsymbol{q}_m \cdot \boldsymbol{x}} U_0(\boldsymbol{q}_c, z; R_c) + A_2(t)\,e^{isx}\,e^{-i\boldsymbol{q}_m \cdot \boldsymbol{x}} U_0(-\boldsymbol{q}_c, z; R_c) + \text{c.c.}, \quad (5.8)$$

with $\boldsymbol{q}_c = (q_c, 0)$ and $s \ll q_c$ and linearize (2.10) about $V_r$ (2.13). Expanding with respect to $Q$ and the Floquet parameter $s$ yields the following coupled equations for the amplitudes $A_i$ (5.8):

$$\tau_0 \partial_t A_1 = \left[ \epsilon - \xi_0^2 (Q + s)^2 \right] A_1 - 2g_0 F_0^2 A_1 - g_0 F_0^2 A_2, \tag{5.9a}$$

$$\tau_0 \partial_t A_2 = \left[ \epsilon - \xi_0^2 (Q - s)^2 \right] A_2 - 2g_0 F_0^2 A_2 - g_0 F_0^2 A_1. \tag{5.9b}$$

The amplitude $F_0 = F_0(Q, \epsilon)$ is again given by (5.5). The ansatz $A_{1,2}(t) \sim e^{\sigma t}$ in (5.9a,b) leads to the growth rate $\sigma(s)$, which has the maximum $s = s_{max}$, when $g_0 F_0^2 \leqslant 2\xi_0^2 Q^2$. We then obtain from the condition $\sigma(s_{max}) = 0$ the following implicit equation for the Eckhaus instability line $\epsilon_E(Q)$:

$$\epsilon_E(Q) = \frac{g_0 F_0^2}{4} \left( 8 - \frac{g_0 F_0^2}{\xi_0^2 Q^2} \right), \quad F_0 = F_0(Q, \epsilon_E(Q)), \tag{5.10}$$

where $\epsilon_E(Q)$ is symmetric in $Q$; a representative example is shown in figure 8. Similar to the previous section, we obtain closed expressions for the coordinates of the turning points $(\pm Q_E^{tp}, \epsilon_E^{tp})$ of $\epsilon_E(Q)$,

$$Q_E^{tp} = \frac{5^{5/6}}{2^{3/2}} \frac{1}{\xi_0} \left( g_2^2 g_0 \right)^{1/6} \delta_m^{1/3}, \quad \epsilon_E^{tp} = \epsilon_E(Q_E^{tp}) = \frac{19}{25} \left( \xi_0 Q_E^{tp} \right)^2, \tag{5.11}$$

which yields $Q_E^{tp} = \pm 2.845 \delta_m^{1/3}$ and $\epsilon_E^{tp} = 0.911 \delta_m^{2/3}$ for $Pr = 1$. A comparison with the turning points of $\epsilon_{ob}$ (5.6) and $\epsilon_{cr}$ (see after (5.7)) reveals the same scaling properties with respect to $\delta_m$. However, a look at the numerical prefactors shows the prevalence of these destabilisation mechanism, as also indicated in figure 8.

### 5.4. *Swift–Hohenberg equation: zigzag instability*

While the Eckhaus instability discussed in §5.3 plays no role for $\delta_m \neq 0$ in our system, this does not apply to the long-wavelength zigzag (ZZ) instability. It is characterized by slow modulations of the rolls along their axes with $\phi = 90°$ in (4.2). The ZZ instability is relevant in unforced RBC, where it restricts the Busse balloon for $Q < 0$ in particular at large $Pr$. The modification of the ZZ instability at finite $\delta_m$ near $q_m \approx q_c$ and $R \approx R_c$ is assessed most easily in the framework of Swift–Hohenberg equations (SHE). This model is very popular to successfully describe patterns of three-dimensional systems mapped onto the two-dimensional $\boldsymbol{x}$-plane by a real order parameter $\psi(\boldsymbol{x}, t)$ (see e.g. Cross & Hohenberg 1993; Cross & Greenside 2009) and for a special application (Buka *et al.* 2004).

We will use a modification of the SHE discussed by Bodenschatz, Pesch & Ahlers (2000, p. 718),

$$\tau_0 \partial_t \psi = \left[ \epsilon - \frac{\xi_0^2}{4q_c^2} \left( \nabla_2^2 + q_c^2 \right)^2 \right] \psi - \frac{g_0}{3} \psi^3 - \frac{1}{q_c^2} (\boldsymbol{U} \cdot \nabla_2) \psi$$
$$+ 2\delta_m (g_2 + \eta \psi) \cos(q_m x), \quad \boldsymbol{U} = (\partial_y G, -\partial_x G, 0), \tag{5.12a}$$

$$\left( c_1 - \frac{c_2 \nabla_2^2}{q_c^2} \right) \nabla_2^2 G = \frac{g_1}{2q_c^2} \left( \nabla_2 (\nabla_2^2 \psi) \times \nabla_2 \psi \right) \cdot \boldsymbol{e}_z, \quad \nabla_2 = (\partial_x, \partial_y, 0). \tag{5.12b}$$

At first, additional terms $\propto \delta_m$, governed by coefficients $\eta$ (A 11) and $g_2$ (3.8), appear in (5.12a) to capture the effect of the external modulation. We have tested that keeping a term $\propto \psi^2$ in (5.12a), which exists in principle due to the broken Boussinesq symmetry for $\delta_m \neq 0$, has no real effect in our anisotropic system. The mean flow (see after (2.8)) is described by $\boldsymbol{U}$, which is determined by the streamfunction $G$.
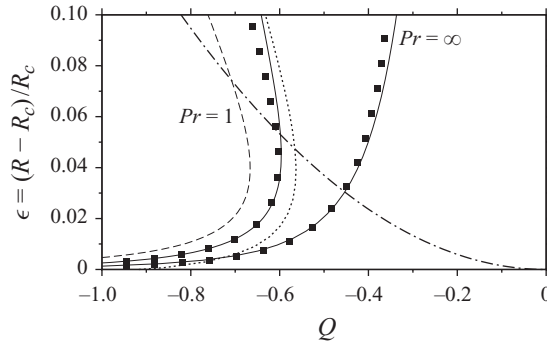
FIGURE 10. Zigzag instability lines for $Pr = 1$ and $Pr = \infty$ (solid) based on (5.12) and the ansatz (5.14) in comparison to the exact Galerkin results (filled squares). The neutral curve (dash-dotted) and both the oblique-roll instability curve from (5.4) (dotted) and $\epsilon_Z(Q)$ (dashed) based on the approximation (5.16) are included for $Pr = 1$.

Apparently, the operator $(c_1 - c_2 \nabla_2^2 / q_c^2)$ can also be identified with the filter operator (denoted as '$F$' in Cross & Hohenberg 1993, p. 969), which has been introduced *ad hoc* to suppress the contributions of fast spatial variations. In Xi, Gunton & Vinals (1993), where (5.12b) has first been introduced, a term $\propto \partial_t \nabla_2^2 G$ also appears, which is not relevant for the ZZ instability. Without loss of generality, we take $c_1 = 1$; the coupling constant $g_1$, which vanishes for $Pr \to \infty$, is given in the Appendix (A 15). The constant $c_2$ has never been calculated directly from the OBE and is typically chosen as $c_2 = 1/2$.

Note that the modified SHE model (5.12) has already been discussed in Manor *et al.* (2008, 2009) for the special case $g_2 = 0$ and $U = 0$. This work, however, does not directly apply to modulated RBC, since a non-zero $g_2$ is necessary for the existence of forced rolls with wavenumber $q_m$. To obtain them, we use for $R \approx R_c$ the ansatz

$$\psi_0(\boldsymbol{x}, t) = F(t) \exp(i\boldsymbol{q}_m \boldsymbol{x}) + \text{c.c.}, \qquad (5.13)$$

which leads to the amplitude equation (3.5) with the stationary solution $F = F_0(q_m, \epsilon)$ given in (3.6a–c).

The oblique-roll perturbations of $\psi_0$ are represented in analogy to (5.1) as a superposition of exponentials $\exp(i\boldsymbol{s}_{1,2} \cdot \boldsymbol{x})$ with amplitudes $A_{1,2}$. In this way, we arrive again at the coupled amplitude equations (5.2a,b), with $\Delta_\epsilon$ given in (A 14), which implies for instance the existence of a stability gap in the SHE.

Let us now concentrate on the long-wavelength ZZ instability, where $c_2 = 0$ in (5.12b) is sufficient. We use in (5.12) the ansatz

$$\delta\psi(\boldsymbol{x}, t) = e^{isy} e^{\sigma t} \left( A_1 e^{i\boldsymbol{q}_m \cdot \boldsymbol{x}} + A_2 e^{i\boldsymbol{q}_m \cdot \boldsymbol{x}} \right) + \text{c.c.} \qquad (5.14)$$

and linearize (5.12) about the forced roll solution $\psi_0$ (5.13). In close analogy to the calculation of the Eckhaus instability in §5.3, we arrive from (5.12) at two coupled equations for the amplitudes $A_i$ and at a lengthy expression for the maximal growth rate $\sigma(s)$. As in §5.3, we have to determine the position $s = s_{max}$ of $\sigma(s)$. The condition $\sigma(s_{max}) = 0$ eventually yields the ZZ instability curve, restricted to negative $Q$, which also shows a turning point. The whole procedure can be done only numerically. In figure 10, the generally good agreement of SHE results (solid curves) and exact Galerkin results (filled squares) is documented at $\delta_m = 0.01$ for $Pr = 1$ and $Pr = \infty$. It is seen that for $Pr = 1$ the oblique-roll instability curve $\epsilon_{ob}(Q)$ (dotted) still determines

the gap of instability. With increasing $Pr$, the ZZ-curve moves to the right and will eventually prevail, since $\epsilon_{ob}$ remains practically unchanged.

The general features of the ZZ instability described above are well reflected in approximate analytical expressions. In the absence of forcing ($\delta_m = 0$), it is sufficient to analyse $\sigma(s)$ in the limit $s \to 0$, which easily yields the ZZ instability line in the regime $Q \lesssim 0$ for medium $Pr$ (see Decker & Pesch 1994):

$$\epsilon_Z^0(Q) = -\frac{\xi_0 q_c g_0}{g_1} \xi_0 Q. \tag{5.15}$$

Thus, the ZZ instability generically preempts for $\delta_m = 0$ the Eckhaus instability $\epsilon_E^0(Q) = 3\xi_0^2 Q^2$.

At finite, small $\delta_m$ the fact that $Q, \epsilon, s_{max}$ and $F_0$ are small as well is exploited by keeping only the leading terms. Then, from the condition $\sigma(s_{max}) = 0$, we obtain the following implicit equation for $\epsilon_Z(Q)$, which is restricted to the regime $Q \leqslant -g_1/(g_0 q_c) g_0 F_0^2 \leqslant 0$:

$$\epsilon_Z(Q) = -\left(2\frac{g_1}{g_0 q_c} Q - 1\right) g_0 F_0^2 - \frac{1}{\xi_0^2}\left(\frac{g_1}{g_0 q_c}\right)^2 g_0^2 F_0^4, \quad F_0 = F_0(Q, \epsilon_Z(Q)), \tag{5.16}$$

where $F_0(Q, \epsilon)$ has to be calculated from (5.5). Starting from (5.16), the coordinates $(Q_Z^{tp}, \epsilon_Z^{tp})$ of the turning point of $\epsilon_Z(Q)$ are given as

$$Q_Z^{tp} = -\frac{5}{2}\frac{1}{\xi_0}\left(\frac{g_1 g_2^2}{8 q_c \xi_0}\right)^{1/5}(\delta_m)^{2/5}, \quad \epsilon_Z^{tp} = \epsilon_Z(Q_Z^{tp}) = -\frac{1}{5}\frac{g_0 q_c \xi_0}{g_1}(\xi_0 Q_Z^{tp}). \tag{5.17}$$

For instance, we have $Q_Z^{tp} = -4.21\, \delta_m^{2/5}$ and $\epsilon_Z^{tp} = 0.100\, \delta_m^{2/5}$ for $Pr = 1$.

According to (5.17) we find $Q_Z^{tp} \sim g_1^{1/5}$ and $\epsilon_Z^{tp} \sim g_1^{-4/5}$; thus, the turning point moves to the right and upwards with increasing $Pr$, i.e. with decreasing $g_1 \sim Pr^{-1}$ (A 15). In the limit $g_1 \to 0$ (i.e. for $Pr \to \infty$) we obtain from (5.16) the following expression for the ZZ instability curve:

$$\epsilon_Z(Q) = \frac{(\delta_m g_2 g_0^{1/2})^2}{(\xi_0 Q)^4}. \tag{5.18}$$

Inspection of (5.17) also shows that $Q_Z^{tp}$ scales as $\delta_m^{2/5}$, whereas both $Q_{ob}^{tp}$ (5.6) and $Q_E^{tp}$ (5.11) scale as $\delta_m^{1/3}$. Thus the ZZ instability must eventually determine the extension of the gap of instability for $Q < 0$ in the limit $\delta_m \to 0$.

In the limit $Pr \to \infty$, where mean-flow effects are absent, the analytical expression for $\epsilon_Z(Q)$ (5.18) would be indistinguishable from the corresponding solid line. This also applies to the case $Pr = 1$ at small $\delta_m \lesssim 0.001$, where it is sufficient to calculate the ZZ instability curve on the basis of (5.16). In contrast, for larger $\delta_m$, as for $\delta_m = 0.01$ in figure 10, the dashed ZZ instability obtained from (5.16) for $Pr = 1$ deviates already considerably from the corresponding solid one.

## 6. The nonlinear regime

The destabilization processes of forced rolls lead to multi-mode patterns, which are characterized by $q_m$ and the wavevectors $s$ of the destabilizing modes. To gain more detailed insight into the resulting patterns, we have performed some numerical simulations of the OBE (2.8), which are presented in this section. On the one hand, we are convincing ourselves that forced rolls with superimposed noise as initial condition are indeed destabilized by the modes that have already been identified in the Galerkin
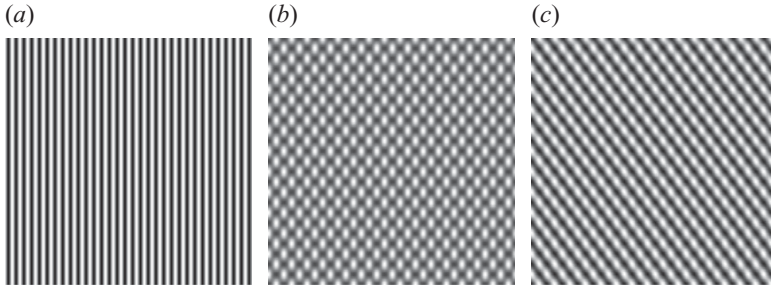
(*a*)  (*b*)  (*c*)



FIGURE 11. Simulations of the OBE (random initial conditions) for $q_m/q_c = 1.6$, $Pr = 1$ and $\delta_m = 0.01$. (*a*) Rolls at $\epsilon = -4.7 \times 10^{-3}$ ($R = 1700$) locked to the external forcing. (*b*) Rectangular pattern at $\epsilon = 0$ ($R = 1708$) consisting of oblique modes with wavevectors $s_{1,2}$ (4.1). (*c*) Oblique-roll pattern at $\epsilon = 7.03 \times 10^{-3}$ ($R = 1720$); the two modes contribute with different weights.

analysis presented in §4. On the other hand we are interested in the final states in the nonlinear regime.

In §6.1 the patterns, which develop for $q_m/q_c$ along the lines OBl and OBr in figure 4 slightly above the oblique-roll bifurcation, have been characterized. The subsequent §6.2 addresses mainly the impact of forcing on SDC for $R > R_c$ and $q_m \approx q_c$. Finally, we demonstrate in §6.3 that much less expensive numerical simulations of the Swift–Hohenberg equations (5.12) are quite powerful to give a first insight into the various aspects of modulated RBC.

### 6.1. *Oblique-roll bifurcation*

The patterns shown in figure 11 for $\delta_m = 0.01$ and $q_m/q_c = 1.6$ are representative of the regime $q_u < q_m < 2q_c$ (line OBr in figure 4). As in general throughout this section, the simulations of the OBE have started from random initial conditions. For sufficiently negative $\epsilon$, forced rolls (figure 11*a*) have developed. According to the Galerkin analysis, they should become unstable against oblique rolls at $\epsilon = \epsilon_{ob} = -8.97 \times 10^{-4}$ with wavevectors $s_{1,2}$ (4.1), forming an angle of about $36.9°$ with the *x*-axis. These wavevectors are perfectly reflected in the stationary 'rectangular' cellular pattern (see figure 11*b*), which has evolved for $\epsilon = 0 \gtrsim \epsilon_{ob}$. The simulation shown in figure 11(*c*) demonstrates, however, that the rectangular pattern is not stable for $\epsilon = 7.03 \times 10^{-3}$, where one of the symmetry-degenerate oblique modes has acquired a larger weight.

The whole scenario is perfectly described by the coupled amplitude equations (5.2*a,b*). Using $\delta_m \eta = 1.0177 \times 10^{-3}$ (A 10) and $\Delta_\epsilon = -0.1189 \times 10^{-3}$ (A 13), we obtain from (5.3) the value $\epsilon_{ob}^A = -0.8988$, which is in excellent agreement with the value from the Galerkin analysis. On the basis of (5.2*a,b*), the resulting rectangular patterns with amplitudes $A_1 = \rho_1 \exp(i\phi)$ and $A_2 = \rho_2 \exp(-i\phi)$ with $\rho_1 = \rho_2$ and arbitrary phase $\phi$ become amplitude unstable ($\rho_1 \neq \rho_2$) at $\epsilon = \epsilon_{as}$, where

$$\epsilon_{as} = 2\delta_m|\eta|/(\gamma' - 1) - \Delta_\epsilon > 0. \tag{6.1}$$

With $\gamma' = 1.559$, one obtains from (6.1) $\epsilon_{as} = 3.522 \times 10^{-3}$ and from (5.2*a,b*) closed expressions for the moduli $\rho_i$ of $A_i$. The whole bifurcation diagram is shown in figure 12; the amplitudes agree almost perfectly with those extracted from figure 11. Note that figure 12 corresponds to figure 2 of Manor *et al.* (2008), which is also based on amplitude equations such as (5.2*a,b*).

For $\eta > 0$, where $A_1 = A_2$ solves (5.1), the pattern varies as $\cos(q_m x/2)\cos(py)$ in the plane; for $\eta < 0$, where $A_1 = -A_2$, the spatial variation is as $\sin(q_m x/2)\sin(py)$.
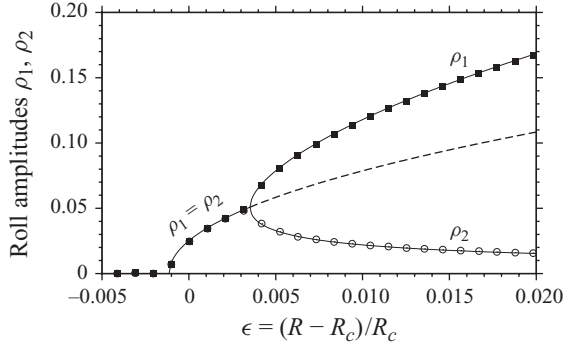
FIGURE 12. Bifurcation diagram for the moduli $\rho_i$ of the oblique modes in figure 11 obtained by solving (5.2a,b) at $q_m/q_c = 1.6$ for $Pr = 1$ and $\delta_m = 0.01$: stable forced rolls $\rho_1 = \rho_2 = 0$ for $\epsilon < \epsilon_{ob} = -0.89 \times 10^{-3}$; stable rectangular patterns $(\rho_1 = \rho_2)$ for $\epsilon_{ob} \leqslant \epsilon \leqslant \epsilon_{as} = 3.522 \times 10^{-3}$; oblique patterns with $\rho_1 \neq \rho_2$ for $\epsilon > \epsilon_{as}$. The filled squares and open circles denote the amplitudes extracted from the simulations in (11) (for details see text).
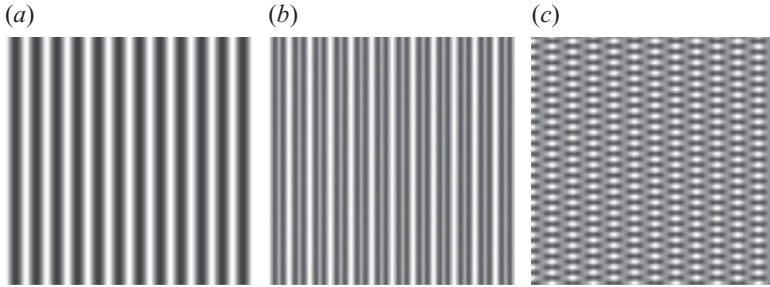


FIGURE 13. Simulations of the OBE (random initial conditions) for $q_m/q_c = 1/2$, $Pr = 1$ and $\delta_m = 0.01$. (a) At $\epsilon = -0.034$ ($R = 1650$), the rolls have locked to the external forcing; (b) forced rolls at $\epsilon = -4.7 \times 10^{-3}$ ($R = 1700$); the $q_c = 2q_m$-contributions (see figure 3) become visible; (c) rectangular patterns at $\epsilon = 0$ ($R = 1708$).

Thus, the rectangular pattern is even (odd) with respect to reflections at the $y$-axis, when $\eta > 0$ ($\eta < 0$). The odd and even solutions become degenerate at $\eta = 0$, which happens at $q_m/q_c \approx 1.92$ in our case. Here $\epsilon_{ob}$, which is only determined by the small coefficient $\Delta_\epsilon \sim 10^{-5}$ (A 13), presents an edge at $\epsilon \approx 0$, as shown in figure 5.

We now briefly address two examples for patterns in the vicinity of the instability curve OBl in figure 5. According to the Galerkin analysis for $\delta_m = 0.01$, $q_m/q_c = 1/2$ and $Pr = 1$, the forced rolls become unstable towards rectangles at $\epsilon_{ob} - 4.03 \times 10^{-3}$. In fact, the direct simulations of the OBE lead in figure 13(a) to stable forced rolls at $\epsilon = -0.034 < \epsilon_{ob}$. Their shadowgraph amplitude $t_1$ has been given in figure 3, where it becomes evident that in the vicinity of $R = R_c$ the amplitude $t_2$ (wavenumber $2q_m = q_c$) starts to grow strongly. The additional longitudinal mode with wavenumber $q_c$ is clearly visible in figure 13(b) for $\epsilon = -4.73 \times 10^{-3} \lesssim \epsilon_{ob}$. As to be expected, the rolls are replaced by rectangles at $\epsilon = 0 > \epsilon_{ob}$ (see figure 13c). When $\epsilon$ increases, however, we do not observe a clear bifurcation to oblique rolls, but instead a mixture between longitudinal and oblique modes, both with wavenumbers $q = q_c$ (not shown).

The situation becomes even more complicated for $q_m/q_c = 1/4$, where $\epsilon_{ob} = -6.9 \times 10^{-3}$. As before, the forced roll solution develops for $\epsilon = -3.4 \times 10^{-2} < \epsilon_{ob}$ (figure 14a). The rolls should be unstable at $\epsilon = 0 > \epsilon_{ob}$. This is confirmed in
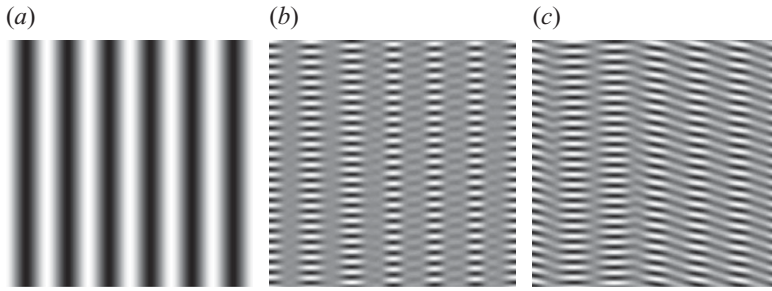
(a)     (b)     (c)



FIGURE 14. Simulations of the OBE (random initial conditions) for $q_m/q_c = 1/4$, $Pr = 1$ and $\delta_m = 0.01$. (a) At $\epsilon = -0.034$ ($R = 1650$), the pattern locks to the external forcing; (b) at $\epsilon = 0$ ($R = 1708$) 'rectangular' patterns with different $x$-periodicity (see text) develop. (c) Oblique-roll pattern at $\epsilon = 7.03 \times 10^{-3}$ ($R = 1720$).

figure 14(b), where a sequence of 'ladders' has replaced the rolls. The ladders are locked to the regions of the locally enhanced temperature gradient in figure 1. However, the pattern is non-uniform along the $x$-axis and consists of two co-existing parts, which are spanned by different modes in Fourier space. On the right, the pattern is mainly built up by modes with wavevectors $(q_m, \pm q_c)$. In contrast, the pattern on the left in figure 14(b) has a rectangular symmetry with wavevectors $s_{1,2} = (q_m/2, \pm p)$ (4.1), which form an angle of about 83° with the $x$-axis. With increasing $\epsilon$, the ladder spokes become wider as shown for $\epsilon = 6.98 \times 10^{-3}$ in figure 14(c). The reflection symmetry in the $y$-direction is obviously broken on the right half of the image, where the Fourier mode with wavevector $s_1 = (q_m, q_c) = (q_c/4, q_c)$ prevails.

## 6.2. *Representative patterns for $q_m/q_c \approx 1$ and $q_m/q_c > 2$*

In this section, we consider some representative simulations for ratios $q_m/q_c$, where the oblique-roll destabilization considered before is not active. We start with the case $q_m/q_c = 1$ for $Pr = 1$. From the stability diagram in figure 4, we expect the forced roll solutions to be stable for $\epsilon < 1.028$ and $\delta_m = 0.01$. This is confirmed in simulations starting from forced rolls, which were slightly perturbed by superimposed small noise. When, however, the forced rolls are unstable at $\epsilon > 1.028$ against SV modes, we observe a transition to spiral-defect chaos (SDC), which evolves and persists even when $\epsilon$ is lowered to an 'under-critical' value ($\epsilon < 1.028$) again. This finding is not too surprising. Even for $\delta_m = 0$, where rolls are linearly stable, it needs special precautions in experiments as well as in simulations to produce ideal roll patterns, since the roll attractor has a small basin of attraction compared with the spatio-temporally chaotic attractor of SDC (see e.g. figure 5 in Bodenschatz *et al.* 2000). Indeed, as shown in figure 15(a), we obtain SDC at $\epsilon = 0.7$ in the absence of forcing when starting from random initial conditions. Apparently, external forcing is an effective tool to control SDC: imposing strong forcing ($\delta_m = 0.1$) in this situation has led to total suppression of SDC and to perfect stationary roll patterns as shown in figure 15(c). In contrast, weaker forcing such as $\delta_m = 0.05$ (see figure 15b) obviously breaks the isotropy, but the pattern still remains disordered due to the presence of dislocations and grain boundaries even in very long runs.

Next, some simulations for the case $q_m = 3q_c$ are presented. For $\epsilon = -4.7 \times 10^{-3}$, the system locks to the forcing and develops $q_c$-rolls as shown in figure 16(a). At $\epsilon = 0$ ($R = R_c$), where rectangular patterns have been found before for $q_m < 2q_c$, the forced roll solution is destabilized by purely transverse rolls (see figure 16b). Since the Rayleigh number is far below the neutral curve $R_0(q_m) = 11\,432$, the amplitude
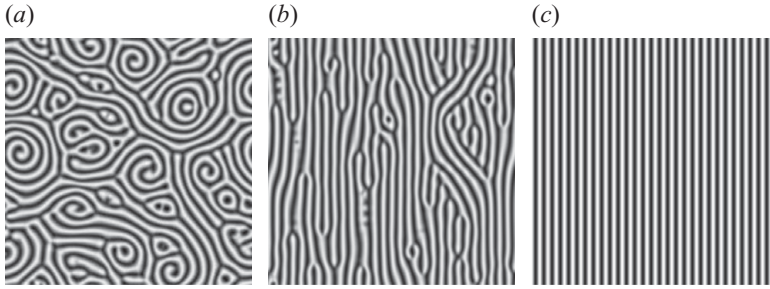
FIGURE 15. Snapshots of OBE simulations for $q_m/q_c = 1$, $Pr = 1$, $\epsilon = 0.7$ ($R = 2904$) and different $\delta_m$. In the absence of forcing, SDC develops ($a$), which is suppressed for $\delta_m = 0.1$ ($c$). Intermediate forcing with $\delta_m = 0.05$ breaks the isotropy ($b$), but is unable to fully suppress spatio-temporal chaos.
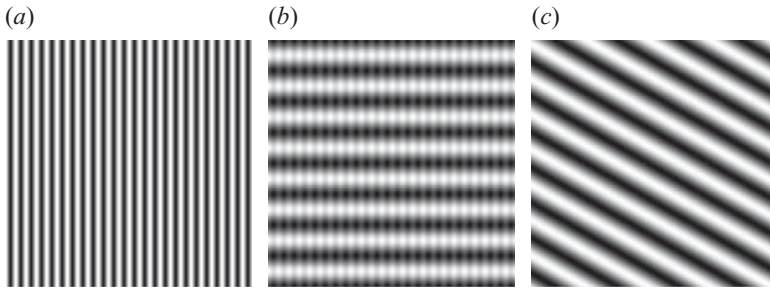


FIGURE 16. Simulations of the OBE (random initial conditions) for $q_m/q_c = 3$, $Pr = 1$, $\delta_m = 0.01$ and different $\epsilon$. ($a$) At $\epsilon = -4.7 \times 10^{-3}$ ($R = 1700$), the pattern has locked to the forcing; ($b$) forced roll solution disturbed by transverse rolls with wavenumber $q_c$ at $\epsilon = 0$ ($R = 1708$); ($c$) oblique rolls with wavenumber $q_c$ at $\epsilon = 4.2 \times 10^{-3}$ ($R = R_c = 1708$).

of the forced roll solution is small. Thus, the impact of the forcing, which breaks in principle the rotational symmetry, is practically negligible. Consequently, for $\epsilon \approx 0$ the growth rate of perturbations with wavevector $s$ ($s = q_c$) varies only slightly with respect to the orientation of $s$. In that respect, it is not too surprising that a simulation for $\epsilon = 4.1 \times 10^{-3}$, starting from random initial conditions, has locked into an oblique-roll pattern as shown in figure 16($c$). Starting at different random initial conditions, other roll orientations have been found as well. It is worth mentioning that we have been unable to detect traces of a subcritical bifurcation to longitudinal $q_c$-rolls, whose existence is to be expected based on very general considerations (see e.g. Hall & Walton 1978; Pal & Kelly 1979; Coullet 1986). Most probably, the hysteresis is very small and the bifurcation to transverse rolls prevails in practice.

### 6.3. *Simulations of the Swift–Hohenberg equations*

In §5.4, we have demonstrated that the Swift–Hohenberg equations (5.12) are well suited to describe the stability diagram of forced rolls for $R \approx R_c$ and for not too large differences $|q_m - q_c|$. In the following, we will illustrate the usefulness of the SHE also in the nonlinear regime by some representative simulations.

At first, we address, in the framework of the SHE, the scenario of the oblique-roll instability as exemplified in the simulations of the OBE shown in figure 11. According to the discussion in §5.4 (see after (5.13)), the bifurcation sequences should be well accessible by the generic amplitude equations (5.2$a,b$) with the use of coefficients $\Delta_\epsilon$
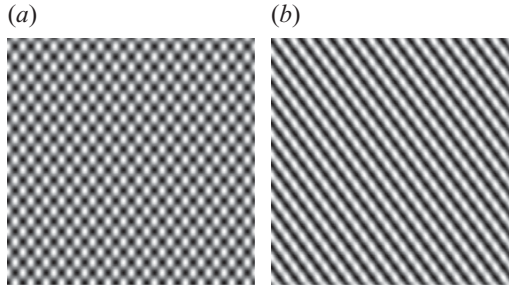
FIGURE 17. Simulations of the SHE (random initial conditions) for $q_m/q_c = 1.6$, $Pr = 1$ and $\delta_m = 0.01$. (a) Rectangular pattern at $\epsilon = 0.001$ and (b) oblique-roll pattern at $\epsilon = 0.01$.
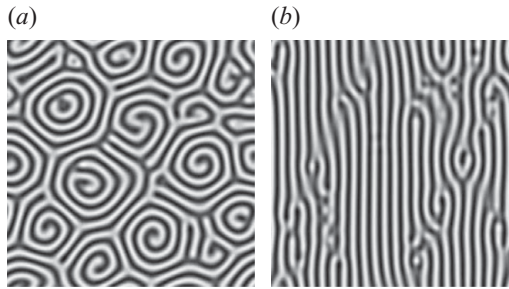


FIGURE 18. Snapshots of the SHE for $Pr = 1$ and $\epsilon = 0.23$. (a) SDC in the absence of forcing and (b) spatio-temporal chaos for finite forcing ($\delta_m = 0.01$).

and $\gamma_{ob} = \gamma' = 2$ for the SHE (see after (A 14) in the Appendix). One obtains for instance the transition points $\epsilon_{ob}^A = -3.022 \times 10^{-3}$ (5.3) from rolls to rectangles and $\epsilon_{as} = 6.11 \times 10^{-3}$ (6.1) from rectangles to oblique rolls. In the SHE simulations, we observe indeed at small $\epsilon < \epsilon_{ob}^A$ stable forced rolls (not shown) as in figure 16(a). At a larger $\epsilon = 0.001 > \epsilon_{ob}^A$, stationary rectangular patterns (see figure 17a) arise, while at $\epsilon = 0.01 > \epsilon_{as}$ one of the oblique rolls prevails (see figure 17c). Note that the mean-flow $U$ is, in general, not excited for regular patterns, such as those shown in figure 17.

As a further example, we address the impact of modulation on SDC within the SHE. It requires a judicious choice of the coefficients of the SHE to produce pictures of SDC which resemble those of the full OBE simulations and the experiments as well. For definiteness, we chose the same coefficients as used in the SDC analysis by Xi *et al.* (1993), which correspond to $g_1 = 12$ and $\epsilon = 0.23$ in our (rescaled version) of the SHE (5.12). Note that $g_1$ is about a factor of 4 larger than $g_1$ for $Pr = 1$ (A 15), while $\epsilon$ is smaller by a factor of about 3 compared to the $\epsilon$ values needed to achieve SDC in full OBE simulations and experiments. In figure 18(a), we present a typical SDC picture in the absence of forcing, which matches the corresponding ones in Xi *et al.* (1993). At finite $\delta_m$, isotropy is broken and we arrive at steady patterns with straight roll patches and additional dislocations as shown in figure 18(b). Increasing $\delta_m$ to 0.1 leads to a perfect roll pattern as in figure 15(c) (not shown).

## 6.4. *Solitary phase modulations*

So far we have concentrated mostly on forced roll solutions of the OBE and their stability in RBC. Forcing has also been applied in experiments on electro-hydrodynamically driven pattern formation. In that generically anisotropic system, a
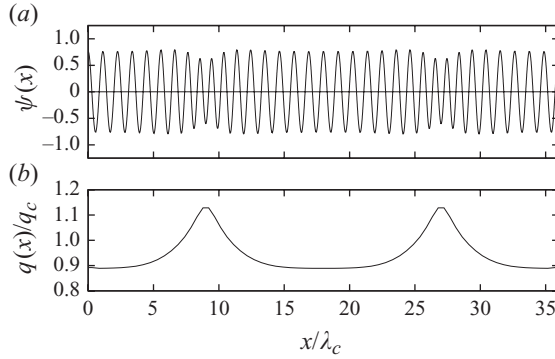
FIGURE 19. Solitary roll structure for the parameters $q_c/q_m = 9/8$, $\epsilon = 0.1$, $\delta_m = 0.01$ and $Pr = 1$: (a) $\psi(x)$ from SHE and (b) local wavenumber $q(x)$ extracted from (a).

preferred direction of the rolls is singled out even in the absence of forcing. Additional forcing may lead to phase-modulated roll patterns, for which the notation 'solitons' has been coined (Lowe & Gollub 1985b). Their theoretical foundation has been laid in the framework of a phase-diffusion model for rolls in RBC (Coullet & Huerre 1986), where one arrives at a sine–Gordon equation.

To keep the numerical effort manageable, we have investigated this scenario in the framework of one-dimensional simulations of the SHE (5.12a). Here the term $\propto \delta_m g_2$ is responsible for the locking of the rolls to the external wavenumber $q_m$. On the other hand, the system has to cope with the disadvantageous wavenumber mismatch $q_c - q_m$, which is reflected in the linear gradient term in (5.12a). As demonstrated in figure 19, the system may indeed make a compromise by producing linearly stable roll solutions with solitary phase modulation: regions of forced rolls with wavenumber $q_m$ are separated by regions with wavenumbers in the vicinity $q_c$. We have chosen the parameters $\epsilon = 0.1$, $\delta_m = 0.01$ and $q_m/q_c = 8/9$ inside the gap of instability (see e.g. figure 7), where uniform forced rolls are stable in the SHE.

Note that the theoretical analysis of Coullet & Huerre (1986) is based on a phase-diffusion equation, where amplitude modulations such as those in figure 19 are adiabatically eliminated. This approach is strictly valid in the limit $\delta_m \to 0$, where the compressed roll regions ($q > q_m$) of the solitons extend over a characteristic length $\sim \sqrt{\delta_m}$. For numerical reasons, we have been unable to address the case of very small $\delta_m$ in the SHE. Furthermore, we emphasize that we did not find two-dimensional 'travelling' solitons in our system, which have been predicted by Coullet & Huerre (1986) as well. For this analysis, the assumption of (non-realistic) free-slip boundary in RBC (entailing Galilean invariance) has been crucial, which leads to a qualitative modification in (5.12b): since $c_1 = 0$ in this case, i.e. $\nabla_2^2 G$ is replaced by $\nabla_2^4 G$.

Solitary structures in the phase of forced rolls have, in fact, also been found in experimental studies of RBC (McCoy et al. 2008; Seiden et al. 2008). In contrast to our case and Lowe & Gollub (1985b), they have appeared only for $q_m > q_c$ and fairly large $\epsilon \sim O(2)$, where neither the SHE nor the phase-diffusion equation in Coullet & Huerre (1986) is directly applicable. In particular, the experimental solitary structures are oriented in an oblique direction with respect to $\boldsymbol{q}_m$ (see FIG 2B (KL) in Seiden et al. 2008). A more sophisticated theory is certainly needed to understand these experimental findings.

## 7. Conclusion

In this paper, we have investigated Rayleigh–Bénard convection, where, in addition to the applied temperature gradient (proportional to the Rayleigh number $R$), a sinusoidal temperature modulation with amplitude $\delta_m$ and wavevector $\boldsymbol{q}_m$ is applied at the lower plate. While in unforced RBC the heat conduction state becomes unstable at the critical Rayleigh number $R_c$ against convection rolls with wavenumber $q_c$, forced roll solutions with wavevector $\boldsymbol{q}_m$ exist at any $R$.

On the basis of the standard OBE, we have presented the first general analysis of forced rolls and their stability regime (the 'Busse balloon'), where we have mainly concentrated on parameters covered by the recent experiments (McCoy *et al.* 2008; Seiden *et al.* 2008).

The various destabilization mechanisms acting on forced rolls depend sensitively on the ratio $q_m/q_c$. We have invested a considerable effort to elucidate these dependencies. In particular, we have made use of suitably constructed amplitude equations. Since they lead to analytical expressions for the stability limits of forced rolls, the consequences of varying the control parameters of the system become immediately obvious. To describe in particular complex multi-mode patterns and their dynamics, we have not only used directly the OBE but also appropriately constructed SHE. As in many other pattern-forming systems, the SHE also give valuable insights in the present case. They describe, for instance, roll patterns with solitary phase modulations, which have been observed in other systems as well.

The various methods exploited in this paper can be generalized to cover other cases as well. First, we plan to address additional spatial forcing at the upper plate. This opens a whole zoo of new possibilities, in particular when the system is frustrated in the presence of non-equal forcing wavenumbers imposed at the two confining plates (see e.g. Schmitz & Zimmermann 1996). Of particular interest is the case of RBC in an inclined fluid layer in the presence of spatial modulation. Here, isotropy is broken even in the absence of forcing and the anisotropy may compete with the external modulation. The many fascinating experimental pictures in Seiden *et al.* (2008, 2009) certainly ask for a systematic theoretical analysis. It should also be mentioned that even in the absence of an applied uniform temperature gradient, a pure temperature modulation leads to periodic convection patterns. This situation also deserves a careful investigation.

We have no doubt that at least the qualitative, generic features of RBC for moderate Rayleigh numbers with *geometric* modulations of the horizontal boundaries of the fluid layer are well accessible in terms of the pure temperature-modulation model investigated in this paper. In fact, the two cases can be directly mapped onto each other for small $\delta_m$ and $R$ in the vicinity of $R_c$ (Kelly & Pal 1978; Seiden *et al.* 2008). Nevertheless, the demanding numerical treatment of geometrically modulated RBC is certainly desirable, to allow for concise quantitative tests. A recent study in this direction by Obé & Khayat (2010) unfortunately suffers from errors and is thus not helpful: the authors have not correctly treated the basic flow and thus have missed, for instance, the characteristic imperfect bifurcation to forced rolls at $q_m \approx q_c$ and $R \approx R_c$.

## Appendix. On the derivation of amplitude equations

In this Appendix, we sketch the 'mode projection' technique to construct amplitude equations and their coefficients in the weakly nonlinear regime $R \gtrsim R_c$. Up to minor technical modifications, we closely follow the calculational scheme proposed by Cross (1980) (for some details see also the Appendix of Plaut & Pesch 1999), which is much easier to handle than the original, quite lengthy multiple-scales perturbation analysis with respect to $\epsilon$ (see e.g. Kelly & Pal 1978).

Since the linear operators $\widehat{\mathscr{B}}$, $\widehat{\mathscr{L}}$ in the OBE (2.10) are not self-adjoint, we have to consider the adjoint eigenvalue problem as well. We use a standard Hermitian scalar product, $\langle\!\langle \cdot | \cdot \rangle\!\rangle$, in position space. For 'vectors' $\widehat{X}(x, z)$, $\widehat{Y}(x, z)$ of the form $e^{iq_1 \cdot x} X(z)$, $e^{iq_2 \cdot x} Y(z)$ we thus obtain

$$\langle\!\langle X | Y \rangle\!\rangle \equiv \delta_{q_1, q_2} \langle X | Y \rangle, \tag{A 1}$$

where $\delta_{q_1, q_2}$ denotes the Kronecker symbol and $\langle \cdot | \cdot \rangle$ is the scalar product

$$\langle X | Y \rangle = \int_{-1/2}^{1/2} dz \, X^*(z) Y(z). \tag{A 2}$$

The adjoint operator $\mathscr{O}^\dagger$ of an operator $\mathscr{O}$ is then, as usual, defined by the relation

$$\langle X | \mathscr{O} Y \rangle = \langle \mathscr{O}^\dagger X | Y \rangle. \tag{A 3}$$

Inspection of the linear problem (2.12) shows that the eigenvectors $U_i^\dagger(q, z)$ of the adjoint problem

$$\sigma_i^*(q, R) \mathscr{C}^\dagger U_i^\dagger(q, z) = \mathscr{L}^\dagger(q, R) U_i^\dagger(q, z) \tag{A 4}$$

obey the boundary conditions (2.9) in $z$ as well, which allows to rely on our standard set of Galerkin functions (see after (2.13)). The eigenvectors of (A 4) fulfil the following generalized orthogonality condition:

$$\sigma_i \langle U_i^\dagger | \mathscr{C} U_j \rangle = \langle U_i^\dagger | \mathscr{L} U_j \rangle = \sigma_i \delta_{i,j}, \tag{A 5}$$

where we have chosen the condition $\langle U_i^\dagger | \mathscr{C} U_i \rangle = 1$ to normalize $U_i^\dagger$.

One important ingredient of the weakly nonlinear analysis after Cross (1980) is to approximate the $z$-dependence of the Fourier coefficients $V(q, z, t)$ in (2.11) in terms of the leading eigenmode $U_0(q, z; R)$ of (2.12). If the pattern is spanned in Fourier space by $L$ modes with wavevectors $q_i$, $i = 1, \ldots, L$, we thus use the ansatz

$$V(q, z, t; R) = \sum_{i=1}^{L} A_i(t) U_0(q, z; R) \delta_{q, q_i}. \tag{A 6}$$

According to (A 5), the expansion coefficients $A_i(t)$ are then obtained as

$$A_i(t) = \langle\!\langle U_0^\dagger(q_i) | \mathscr{C} \, e^{-iq_i \cdot x} \widehat{V} \rangle\!\rangle. \tag{A 7}$$

By inserting (2.11) with $V(q)$ from (A 6) into (2.10), followed by a systematic expansion up to cubic order in $A_i$, one arrives at the familiar coupled amplitude equations for $A_i$ in the weakly nonlinear regime ($R \gtrsim R_c$). For $L = 2$ and wavevectors $q_1$ and $q_2$ of modulus $|q_i| = q_c$, they have the following form (see e.g. (4.30) in Cross & Hohenberg 1993):

$$\tau_0 \partial_t A_1(t) = \epsilon A_1(t) - g_0 A_1 |A_1|^2 - \gamma(\beta) g_0 A_1 |A_2|^2; \qquad (A 8)$$

the equation for $A_2$ follows from (A 8) by interchanging $1 \leftrightarrow 2$.

The coefficient $g_0$, already given in (3.8), can be found in Cross & Hohenberg (1993). The *cross-coefficient* $\gamma(\beta)$ depends on the angle $\beta$ between $q_1$ and $q_2$ (i.e. $\cos \beta = q_1 \cdot q_2 / q_c^2$) and on the Prandtl number. Here $\gamma(\beta)$ is an even function of $\cos(\beta)$, which decreases monotonically with increasing $\beta$, $0 < \beta < 90°$. The original calculation of $\gamma(\beta)$ in Schlüter, Lortz & Busse (1965) for RBC has been considerably simplified by Cross (1980); see also Cross & Hohenberg (1993, pp. 877 and 966).

In the case of forcing ($\delta_m \neq 0$), we need in addition the coefficient $g_2$ in (3.5). It is calculated by projecting the term $\delta_m R \hat{I}$ in (2.10) on $U_0(q_m)$,

$$\hat{g}_2(q_m, R) = R \langle U_0(q_m, R) | t_m(q_m) \rangle, \qquad (A 9)$$

which yields $g_2 = \tau_0 \hat{g}_2(q_c, R_c) = 0.633$ given in (3.8).

To calculate the coefficients $\eta$ and $\Delta_\epsilon$ in (5.2a,b), we introduce the perturbation $\delta \widehat{V}_{ob}$ (5.1) into the OBE (2.10) and linearize about the forced roll solution $\widehat{V}_r(x, z)$ (2.13). Then, we easily obtain for the coefficient $\eta$ the expression $\eta = \hat{\eta} \tau_0 / \delta_m$, where

$$\hat{\eta} = \langle U_0(s_1) | N[V_r(q_m, z), U_0(-s_2, z, R_c)] + N[U_0(-s_2, z; R_c), V_r(q_m, z))$$

$$+ \delta_m R_c N_m[U_0(-s_2, z), t_m(q_m, z)] \rangle. \quad (A 10)$$

Here $V_r(q_m, z)$ denotes the Fourier coefficient of $\widehat{V}_r(x, z)$, as defined in (2.13). The value of $\eta$ at $q_m = q_c$, which is needed in (5.4) and (5.12a), is given by

$$\eta = 0.2915 + 0.034/Pr - (0.3015 + 0.058/Pr + 0.018/Pr^2)\delta_m^{2/3} + O(\delta_m^{4/3}), \quad (A 11)$$

which has been obtained by a fit to the numerical results from (A 10). To understand the origin of the terms such as $\propto \delta_m^{2/3}$, one has to realize that only the odd-in-$z$ part of $V_r(q_m, z)$, which vanishes in the limit $\delta_m \to 0$, contributes to $\eta$ in (A 10). This part can be satisfactorily represented as a power series in $F_0^2 \propto \delta_m^{2/3}$ at $q_m = q_c$ and $\epsilon = 0$ (see (5.5)).

The calculation of $\Delta_\epsilon$ is more complicated. At first, we need in an intermediate step the fields $V_2(s_i \pm q_m, z)$, which arise from the combination of $\delta \widehat{V}_{ob}$ and the roll solution $\widehat{V}_r$ transformed to Fourier space. According to (2.10), we have to solve

$$\mathcal{L}(s_i \pm q_m) V_2(s_i \pm q_m) = N[V_r(\pm q_m), U_0(s_i)] + N[U_0(s_i), V_r(\pm q_m)], \quad (A 12)$$

where we have again suppressed the $z$- and the $R$-dependences. Note that for instance the wavevector combination $s_1 - q_m$ with modulus $q_c$ must be treated with care (see Plaut & Pesch 1999). The required solution of (A 12) has to be restricted to the

subspace orthogonal to $U_0(s_1 - q_m)$, since the component proportional to $U_0(s_1 - q_m)$ has already been captured by the $A_2^*$ term in the ansatz (5.1). Combining the solutions $V_2$ with $V_r(q_m)$, we obtain $\Delta_\epsilon = \tau_0 \Delta'_\epsilon$ from (2.10), where

$$
\begin{aligned}
\Delta'_\epsilon = \langle U_0(s_1) | ( &N[V_2(s_1 + q_m), V_r(-q_m)] + N[V_r(-q_m), V_2(s_1 + q_m)] \\
&+ N[V_2(s_1 - q_m), V_r(q_m)] + N[V_r(q_m), V_2(s_1 - q_m)] \\
&+ N[U_0(s_1), V_0(0)] + N[V_0(0), U_0(s_1)] \\
&+ \delta_m N_m[V_2(s_1 + q_m), t_m(-q_m)] + \delta_m N_m[t_m(-q_m), V_2(s_1 + q_m)] ) \rangle.
\end{aligned}
\tag{A 13}
$$

In the regimes $0 < q_m < q_l$ and $q_l < q_m < 2q_c$, it is sufficient to use the Fourier coefficient $V_r(q_m, z, R)$ at $R = R_c$. This approximation is insufficient for $q_m \approx q_c$. Here we have used $V_r(q_m, z; R) = F_0(q_m, R) U_0(q_m, z; R_c)$, where the amplitude $F_0(q_m, R)$ is determined by (5.5). The terms $\propto t_m$ (2.4) in (A 13) are negligible in this case. A closer look at Cross (1980) shows that the remaining terms in (A 13) already appear in the calculation of the cross-coefficient $\gamma(\beta)$ defined in (A 8). In the present case, we have $q_1 = q_m = (q_c, 0)$ and $q_2 = s_2$ (4.1), which form an angle of $\beta = 60°$. Thus, we obtain

$$
\Delta_\epsilon = -\gamma_{ob} g_0 |F_0|^2,
\tag{A 14}
$$

where $\gamma_{ob} \equiv \gamma(60°) = 1.658$ for $Pr = 1$. In the framework of the SHE, the cross-coupling coefficient $\gamma(\beta)$ (A 8) is derived by simply generalizing the ansatz (5.13) to two modes. Thus, one arrives easily at the $\beta$-independent value $\gamma(\beta) \equiv \gamma_{SH} = 2$, which replaces for instance $\gamma_{ob}$ in the calculation of $\Delta_\epsilon$ in (A 14).

The coupling constant $g_1$ in (5.12b), which depends on $Pr$, has been derived systematically from the OBE and is given as (see Decker & Pesch 1994)

$$
g_1 = \frac{\xi_0^2 g_0 q_c^2}{Pr} \frac{1 + 0.34291 Pr^{-1}}{0.497684 - 0.003355 Pr^{-1} + 0.005921 Pr^{-2}}.
\tag{A 15}
$$

With the use of (A 15) one obtains excellent agreement of the ZZ instability line $\epsilon_Z^0(Q)$ (5.15) with the exact result first given by Manneville & Piquemal (1983). To get quantitative agreement, one has to include certain additional terms into (5.12a), e.g. cubic gradient terms (see Decker & Pesch 1994). In this way, one is also able to restore the angle-dependence of the cross-coefficients $\gamma(\beta)$ in the SHE to some extent (see e.g. Buka *et al.* 2004).

## REFERENCES

BODENSCHATZ, E., PESCH, W. & AHLERS, G. 2000 Recent developments in Rayleigh–Bénard convection. *Annu. Rev. Fluid Mech.* **32**, 709–778.

BUKA, A., DRESSEL, B., KRAMER, L. & PESCH, W. 2004 Direct transition to electroconvection in a homeotropic nematic liquid crystal. *Chaos* **14**, 793–802.

BUSSE, F. H. & CLEVER, R. M. 1979 Instabilities of convection rolls in a fluid of moderate Prandtl number. *J. Fluid Mech.* **91**, 319–335.

BUSSE, F. H. & WHITEHEAD, J. A. 1971 Instabilities of convection rolls in a high Prandtl number fluid. *J. Fluid Mech.* **47**, 305–320.

CHANDRASEKHAR, S. 1961 *Hydrodynamic and Hydromagnetic Stability*. Dover.

CHIAM, K. H., PAUL, M. R., CROSS, M. C. & GREENSIDE, H. S. 2003 Mean flow and spiral defect chaos in Rayleigh–Bénard convection. *Phys. Rev.* E **67**, 056206.

CLEVER, R. M. & BUSSE, F. H. 1974 Transition to time-dependent convection. *J. Fluid Mech.* **65**, 625–645.

COULLET, P. 1986 Commensurate–incommensurate transition in nonequilibrium systems. *Phys. Rev. Lett.* **56**, 724–727.

COULLET, P. & HUERRE, P. 1986 Resonance and phase solitons in spatially forced thermal convection. *Physica* D **23**, 27–44.

CROSS, M. C. 1980 Derivation of the amplitude equation at the Rayleigh–Bénard instability. *Phys. Fluids* **23**, 1727–1731.

CROSS, M. C. & GREENSIDE, H. 2009 *Pattern Formation and Dynamics in Nonequilibrium Systems*. Cambridge University Press.

CROSS, M. C. & HOHENBERG, P. C. 1993 Pattern formation outside of equilibrium. *Rev. Mod. Phys.* **65**, 851–1112.

DECKER, W. & PESCH, W. 1994 Order parameter and amplitude equations for the Rayleigh–Bénard convection. *J. Phys.* II **4**, 419–438.

HALL, P. & WALTON, I. C. 1978 The smooth transition to a convective regime in a two-dimensional box. *Proc. R. Soc. Lond.* A **358**, 199–221.

HENRIOT, M., BURGUETE, J. & RIBOTTA, R. 2003 Entrainment of a spatially extended nonlinear structure under selective forcing. *Phys. Rev. Lett.* **91**, 104501.

KELLY, R. E. 1993 Thermal convection in fluid layers with nonuniform thickness or surface temperature. In *IUTAM Symp. on Nonlinear Instability of Nonparallel Flows* (ed. S. P. Lin, W. R. C. Phillips & D. T. Valentine), pp. 1–12. Springer.

KELLY, R. E. & PAL, D. 1976 Thermal convection induced between non-uniformly heated horizontal surfaces. In *Proc. 1976 Heat Transfer and Fluid Mechanics Institute* (ed. A. A. McKillop, J. W. Baughn & H. A. Dwyer), pp. 1–17. Stanford University Press.

KELLY, R. E. & PAL, D. 1978 Thermal convection with spatially periodic boundary conditions: resonant wavelength excitation. *J. Fluid Mech.* **86**, 433–456.

LOWE, M. & GOLLUB, J. P. 1985a Pattern selection near the onset of convection: the Eckhaus instability. *Phys. Rev. Lett.* **55**, 2575–2578.

LOWE, M. & GOLLUB, J. P. 1985b Solitons and the commensurate–incommensurate transition in a convecting nematic fluid. *Phys. Rev.* A **31**, 3893–3897.

MANNEVILLE, P. & PIQUEMAL, J. M. 1983 Zigzag instability and axisymmetric rolls in Rayleigh–Bénard convection: the effects of curvature. *Phys. Rev.* A **28**, 1774–1790.

MANOR, R., HAGBERG, A. & MERON, E. 2008 Wavenumber locking in spatially forced pattern-forming systems. *Europhys. Lett.* **83**, 10005.

MANOR, R., HAGBERG, A. & MERON, E. 2009 Wavenumber locking and pattern formation in spatially forced systems. *New J. Phys.* **11**, 063016.

MCCOY, J. 2008 Pattern formation due to spatially periodic forcing. PhD thesis, Cornell University.

MCCOY, J. H., BRUNNER, W., PESCH, W. & BODENSCHATZ, E. 2008 Self-organization of topological defects due to applied constraints. *Phys. Rev. Lett.* **101**, 254102.

OBÉ, M. & KHAYAT, R. E. 2010 Spatially modulated thermal convection. *Intl J. Numer. Meth. Heat Fluid Flow* **20**, 17–36.

PAL, D. & KELLY, R. E. 1979 Three-dimensional thermal convection produced by two-dimensional thermal forcing. In *Proc. Joint ASME/AIChE 18th Natl Heat Transfer Conf., San Diego, California, 1979*, pp. 1–8. *ASME* 79-HT-109.

PESCH, W. 1996 Complex spatiotemporal convection patterns. *Chaos* **6**, 348–357.

PLAUT, E. & PESCH, W. 1999 Extended weakly nonlinear theory of planar nematic convection. *Phys. Rev.* E **59**, 1747–1769.

SCHLÜTER, A., LORTZ, D. & BUSSE, F. 1965 On the stability of steady finite amplitude convection. *J. Fluid Mech.* **23**, 129–144.

SCHMITZ, R. & ZIMMERMANN, W. 1996 Spatially periodic modulated Rayleigh–Bénard convection. *Phys. Rev.* E **53**, 5993–6011.

SEIDEN, G., WEISS, S. & BODENSCHATZ, E. 2009 Superlattice patterns in forced thermal convection. *Chaos* **19**, 041102.

SEIDEN, G., WEISS, S., MCCOY, J. H., PESCH, W. & BODENSCHATZ, E. 2008 Pattern forming system in the presence of different symmetry-breaking mechanisms. *Phys. Rev. Lett.* **101**, 214503.

SEMWOGERERE, D. & SCHATZ, M. F. 2002 Evolution of hexagonal patterns from controlled initial conditions in a Bénard–Marangoni convection experiment. *Phys. Rev. Lett.* **88**, 054501.

TRAINOFF, S. P. & CANNELL, D. S. 2002 Physical optics treatment of the shadowgraph. *Phys. Fluids* **14**, 1340–1363.

Vozovoi, L. P. & Nepomnyashchy, A. A. 1974 Convection in a horizontal layer in the presence of spatial modulation of temperature at the boundaries. *Gidrodinamika* **7**, 105–117 (published by the Governmental Pedagogical Institute of the University of Perm, Russia).

Weiss, S. 2009 On forcing in thermal convection experiments. PhD thesis, Universität Göttingen.

Xi, H. W., Gunton, J. D. & Vinals, J. 1993 Spiral defect chaos in a model of Rayleigh–Bénard convection. *Phys. Rev. Lett.* **71** (13), 2030–2033.

Zimmermann, W., Ogawa, A., Kai, S., Kawasaki, K. & Kawakatsu, T. 1993 Wavelength competition in convective systems. *Europhys. Lett.* **24**, 217–222.